NANOSILICA BASED 3D PRINTED SCAFFOLD

FACILITATE

OSTEOBLAST MINERAL FORMATION

by

TUGBA CEBE

THESIS

Submitted in partial fulfillment of the requirements

for the degree of Master of Science in Material Science and Engineering at

The University of Texas at Arlington

August 2017

Arlington, Texas

Supervising Committee:

Dr. Pranesh B. Aswath

Dr. Pelagia Irena Gouma

Dr. Panos S. Shiakolas

Dr. Venu Varanasi

Copyright by

Tugba CEBE of Author 2017

ACKNOWLEDGEMENT

I am thankful to many people who have contributed, through their support, inspiration, knowledge, encouragement and friendship throughout my master studies, to bring this thesis to completion. I would first like to thank my advisor, Prof. Pranesh B. Aswath, who gave me the opportunity to join this wonderful group. It is very difficult for me to overstate my gratitude to Prof. Venu Varanasi, without whose inspirational and expert guidance, constant encouragement and endless help, I would never have finished this master degree. I will always be grateful for Dr. Aswath and Dr. Varanasi's suggestions, which not only enriched my breadth of knowledge but also helped in maintaining my future efforts.

I sincerely acknowledge Prof. Pelagia Irene Gouma, one of my master committee members, for her valuable assistance. I also take this opportunity to thank the other master committee members, including Dr. Panos S. Shiakolas, for their helpful advice and suggestions.

I sincerely acknowledge Dr. Danieli Rodrigues for allowing the use of her laboratory for rheological property experiments at the University of Texas at Dallas and her PhD student Danyal Siddiqui for his assistance during the tests.

I truly acknowledge Dr. Felipe Monte and Vinay Sharma, in addition to being my friends, provided their valuable assistance, suggestions and fruitful discussions on my research and related techniques.

I would like to acknowledge my fellow graduate students and friends Kamal Rashad Ibrahim Awad, Neelam Ahuja, Ami Shah, and Dr. Chi Ma, Bei, Zachi in Dr. Xiaohua Liu's laboratory at the Texas A&M College of Dentistry, and Prashanth Ravi, Phillip Zachary James in Dr. Shiakolas's laboratory as well as several others for their time, suggestions and fruitful

discussions. Finally, I sincerely thank my parents and other family members for their love, support and encouragement. I am also grateful to my parents and my brothers and sister, who always have been with me throughout this endeavor.

August 2017

LIST OF ILLUSTRATIONS

Figure 1.1 Basic chemical structure of gelatin

Figure 1.2 Basic chemical structure of chitosan

Figure 1.3 (a) Empirical formula of laponite, and (b) Idealized structural formula of Laponite, and (c) Single Laponite platelet

Figure 1.4 Schematic of the three methods of crosslinking. (a) Chemical crosslinking with the crosslinker incorporated into the bond. (b) Chemical crosslinking with the crosslinker not incorporated into the bond. (c) Physical crosslinking

Figure 1.5 Photocrosslinking process of MAG

Figure 1.6 Schematic of the basic principles of tissue engineering by using hydrogels as an extracellular matrix

Figure 1.7 Schematic diagram of the scaffold prepared using the layer-by-layer 3D robocasting technique. (a) The 3D robocasting machine. Inside is drawing of the extrusion equipment (b-g) The schematic diagram of the printing process of the scaffold

Figure 3.1 Synthesis of methacrylated gelatin. (a) Gelatin macromers containing primary amine groups were reacted with methacrylic anhydride (MA). (b) To create a hydrogel network, the methacrylated gelatin was crosslinked using UV irradiation in the presence of a photoinitiator

Figure 3.2 Schematic illustration of methacrylated gelatin synthesis

Figure 3.3 Chitosan [1] primary amine groups react with methacrylic anhydride to produce methacrylamide chitosan (MAC) [2]. Free radical polymerization of MAC on the methacrylamide group

Figure 3.4 Schematic illustration of methacrylated chitosan synthesis

Figure 3.5 Schematic illustration of MAG-Lp ink preparation

Figure 3.6 Schematic illustration of MAC-Lp ink preparation

Figure 4.1 (a) FTIR results of gelatin and MAG range between 4000 and 500 cm^{-1}. (b) FTIR results with zoom version within range of 2000 to 500 cm^{-1}

Figure 4.2 (a) FTIR results of gelatin and MAG range between 4000 and 500 cm^{-1}. (b) FTIR results with zoom version within a range of 2000 to 500 cm^{-1}

Figure 4.3 Gross shape of MAG and MAC products. Left ones are MAG, and the right ones are MAC.

Figure 4.4 Storage Modulus (G′) and Loss Modulus (G″) for MAC, MAC-Lp, MAG, MAG-Lp inks

Figure 4.5 Viscosity properties for MAC, MAC-Lp, MAG, MAG-Lp inks

Figure 4.6 The gross shape of the bio-ink scaffold. The resolution of pores in the scaffold 450±50μm

Figure 4.7 Effect of real-time UV illumination intensity on scaffolds immersed with α - MEM (Day 1). First group is MAC-Lp, second is MAG-Lp.

Figure 4.8 Effect of real-time UV illumination intensity on scaffolds immersed with α - MEM (Day 28). First group is MAC-Lp, second is MAG-Lp.

Figure 4.9 Photopolymerization with UV light during printing scaffolds

Figure 4.10 Mechanical properties of MAG-Lp 30 mW/cm^2, MAC-Lp 30 mW/cm^2, and MAC-Lp 40 mW/cm^2. Specimen name 1 is MAG-Lp 30 mW/cm^2, name 2 is MAC-Lp 30 mW/cm2, and Specimen name 3 is MAC-Lp 40 mW/cm^2.

Figure 4.11 Graphical demonstrations of mechanical properties of all scaffold groups

Figure 4.12 Various magnifications with Stereo Zoom Microscope images of MAC and MAC-Lp scaffolds.

Figure 4.13 Various magnifications with Stereo Zoom Microscope images of MAG and MAG-Lp scaffolds.

Figure 4.14 Scanning Electron Microscope (SEM) images of MAC-Lp scaffolds, 25 kV voltage, ×30, ×45 and ×60 magnifications

Figure 4.15 Porous size of MAC-Lp scaffold. Average filament size was 118.5±12.19 μm. The pore sizes were 389 ± 58 μm based on horizontal, 385±38 μm based on vertical.

Figure 4.16 Scanning Electron Microscope (SEM) images of MAG-Lp scaffolds, 25 kV voltage, ×40, ×50 and ×80 magnifications

Figure 4.17 Porous size of MAG-Lp scaffold. Average filament size was 267.5± 23 μm. The pore sizes were 530± 21 μm based on horizontal, 450 ± 25 μm based on vertical

Figure 4.18 Cell attachment to tissue culture plate a) 10× magnification Phalloidin 488 (actin), b) 10× magnification DAPI, c) 10× magnification combined with Phalloidin 488 (actin) and DAPI

Figure 4.19 Various magnifications of cell attachment MAC-Lp scaffolds. a) 5× bright field, b) 5× DAPI, c) 5X- Phalloidin 488 (actin), d) 20× Combined with DAPI and Phalloidin 488 (actin), e) 10× Phalloidin 488 (actin), f) 10× Phalloidin 488 (actin), g) 40× Phalloidin 488 (actin), h) 40× Phalloidin 488 (actin)

Figure 4.20 Various magnifications of cell attachment MAC-Lp scaffolds. a) 5× bright field, b) 5× DAPI, c) 5×- Phalloidin 488 (actin), d) 20× Combined with DAPI and Phalloidin 488 (actin), e) 10× Phalloidin 488 (actin), f) 10× Phalloidin 488 (actin), g) 40× Phalloidin 488 (actin), h) 40× Phalloidin 488 (actin)

Figure 4.21 Cell viability of the MC3T3-E1 subclone 4 cell with tissue culture plate and scaffold groups which are MAG, MAG-Lp, MAC, MAC-Lp, viability 1 day ***$p<0.001$ n=6/group

Figure 4.22 Relative cell growth of the MC3T3-E1 subclone 4 cell with tissue culture plate and scaffold groups, proliferation 1 day #p<0.05 n=6/group

Figure 4.23 Relative cell growth of the MC3T3-E1 subclone 4 cell with tissue culture plate and scaffold groups, proliferation 3 days, **p<0.01 *p<0.05 n=6/group

Figure 4.24 Relative cell growth of the MC3T3-E1 subclone 4 cell with tissue culture plate and scaffold groups, proliferation 7 days, **p<0.01 *p<0.05 n=6/group

Figure 4.25 ECM collagen [1]

Figure 4.26 Collagen fiber in MAC-Lp scaffold

Figure 4.27 FTIR results for MAC-Lp and MAC scaffolds after 28 days matrix deposition. a) MAC-Lp scaffolds, and b) MAC scaffolds

Figure 4.28 FTIR results for MAG-Lp and MAG scaffolds after 28 days matrix deposition. a) MAG-Lp scaffolds and b) MAG scaffolds

Figure 4.29 FTIR results for MAC-Lp, MAC, MAG-Lp and MAG scaffolds after 28 days matrix deposition

Figure 4.30 Raman result for MAC-Lp scaffolds. It was shown that there was phosphate, Amide I and Amide III bands.

LIST OF TABLES

Table 3.1 Schematic diagram of temperature, time, and speed for MAG, MAG-Lp, MAC, and MAC-Lp scaffolds

Table 3.2 Schematic diagram of debubbling time, and speed for MAG, MAG-Lp, MAC, and MAC-Lp scaffolds

Table 4.1 Schematic diagram of temperature, time, and speed for MAG, MAG-Lp, MAC, and MAC-Lp scaffolds

Table 4.2 Attempts to evaluate the optimum distance between substrate and dispenser tip for MAG and MAG-Lp

Table 4.3 Attempts to evaluate the optimum distance between substrate and dispenser tip MAC and MAC-Lp

Table 4.4 Schematic diagram of various UV intensities for MAG-Lp and MAC-Lp

Table 4.5 % swelling of MAG with different compositions after immersion in DPBS

Table 4.6 % swelling of MAG-Lp with different compositions after immersion in DPBS

Table 4.7 % swelling of MAC with different compositions after immersion in DPBS

Table 4.8 % swelling of MAC-Lp with different compositions after immersion in DPBS

Table 4.9 Compressive strength values (n=3) for MAG, MAG-Lp, MAC, and MAC-Lp scaffolds with averages, and standard deviations

Table 4.10 Averages and standard deviations of mechanical properties of MAG, MAG-Lp, MAC and MAC-Lp discs

Table 4.11 Averages and standard deviations of MAC-Lp scaffold based on horizontal and vertical

Table 4.12 Averages and standard deviations of MAG-Lp scaffold based on horizontal and

vertical

Table 4.13 Phosphate and Amide I ratio of FTIR results for MAC-Lp, MAC, MAG-Lp and MAG

LIST OF ABBREVIATONS

MAC Methacrylated Chitosan ink of 10% MAC, and 0.8% I2959 2% acetic acid

MAC-Lp Methacrylated Chitosan with Laponite ink of 4% wt Lp, 10% wt MAC, 2% wt Suc, and 0.8% wt I2959 2% acetic acid

MAG Methacrylated Gelatin ink 20% MAG, and 0.8% I2959

MAG-Lp Methacrylated Gelatin with Laponite ink of 4% LP, 20% MAG, 2% Suc, and 0.8% I2959

2D Two Dimensional

3D Three Dimensional

3DP 3-Dimensional Printing

α-MEM Alpha modified Minimum Essential Media

BMP Bone Morphogenetic Protein

Ca Calcium

CAD Computer Aided Design

CAM Computer Aided Manufacturing

CCMB Characterization Center for Material and Biology

CSD Critical Size Defects

DAPI 4',6-Diamideino-2-Phenylindole

DPBS Dulbecco's Phosphate Buffered Saline

ECM Extra Cellular Matrix

EDS Energy-Dispersive X-ray Spectroscopy

EtOH Ethanol

FBS Fetal Bovine Serum

FTIR Fourier Transform Infrared Spectroscopy

HA HydroxyApatite

I2959 IRGACURE 2959

Krpm Kilo Revolutions Per Minute LP Laponite

MA Methacrylate Anhydride

MTS (3-(4,5-dimethylthiazol-2-yl)-5-(3-carboxymethoxyphenyl)-2-(4-sulfophenyl)-2H-tetrazolium)

N/A Not applicable

NH_3 Amino chemical group

O Oxygen

OH Hydroxyl chemical group

P Phosphorous

DPBS Dubecco Phosphate Buffered Saline

PCL Poly Caprolactone

PLA Poly Lactic Acid should be PLLA

PGA Poly Glycolic Acid

PLGA Poly Lactic-co-Glycolic Acid

RGD Arginylglycylaspartic acid

RP Rapid Prototyping

rpm Revolution Per Minute

RUNX2 Runt-related Transcription Factor 2

SEI Secondry Electron Imaging

SEM Scanning Electron Microscopy imaging

Si^{+4} Silicon ion with a charge of +4

Suc Sucrose

TCP Tri-Calcium Phosphate

UV Ultra Violet light

XRD X-Ray Diffractometer

Table of Contents

ACKNOWLEDGEMENT iii

LIST OF ILLUSTRATIONS v

LIST OF TABLES ix

LIST OF ABBREVIATONS xi

ABSTRACT xvii

CHAPTER 1 1

GENERAL INTRODUCTION 1

1.1 Bone and grafting 1

1.2 Biomaterials 2

1.3 Hydrogel 2

1.4 Gelatin 3

1.5 Chitosan 4

1.6 Bioceramic 6

1.7 Laponite 7

1.8 Crosslinking Mechanism 9

1.9 Photopolymerization 10

1.10 Applications of Hydrogel 11

1.10.1 Tissue Engineering 11

1.11 Additive Manufacturing – Robocasting 12

1.12 Aim of thesis 14

CHAPTER 2 16

PAPER 1 16

1. Abstract 17

2. Introduction 18

3.1 Methacrylated Gelatin Synthesis 19

3.2 Methacrylated Chitosan Synthesis 20

3.3 Injectability Evaluation 22

3.4 Scaffold Composition and Ink Preparation 22

3.4.1 Methacrylated Gelatin 23
3.4.3 Methacrylated Chitosan 24
3.4.4 Methacrylated Chitosan and Laponite 24
3.5 Rheological and Dynamic Mechanical Properties 25

3.6 Adjusting Printing Setting 26

3.7 Minimum UV Intensity for Ink Crosslinking 28

3.8 Swelling Test 28

3.9 Mechanical Test 29

3.10 Scaffold Surface Analysis 30

3.11 Control Media Preparation and Cell Culture 31

3.11.1 Cell Attachment 31
3.11.2 Cell Viability 32
3.11.3 Cell Proliferation 32
3.11.4 Extra Cellular Matrix - Collagen Fiber 32
3.12 Fourier Transform Infrared Spectroscopy for Osteoblast Formation 33

3.13 Raman Analysis of MAC-Lp scaffold for Osteoblast Formation 33

RESULTS AND DISCUSSION 35

4.1 Methacrylated Gelatin Synthesis 35

4.2 Methacrylated Chitosan Synthesis 36

4.4 Rheological Properties and Dynamic Mechanical Properties 37

4.5 Adjusting Material and Printing Setting 39

4.6 Minimum UV Intensity for Ink Crosslinking 41

4.7 Swelling Test 43

4.8 Mechanical Properties 44

4.9 Scaffold Surface Analysis 46

4.9.2 Cell Viability 52
4.9.3 Cell Proliferation 53
4.9.4 Collagen Analysis by SEM 55
4.10 Fourier Transform Infrared Spectroscopy for Osteoblast Formation 56
4.11 Raman Spectroscopy of MAC-Lp Scaffolds for Osteoblast Formation 59
4.12 SEM – EDS of MAC-Lp Scaffolds for Osteoblast Formation 61

CHAPTER 3 63

CONCLUSION 63

REFERENCES 65

ABSTRACT

NANOSILICA BASED 3D PRINTED SCAFFOLD

FACILITATE

OSTEOBLAST MINERAL FORMATION

Tugba Cebe, MS

The University of Texas at Arlington, 2017

Supervising Professor: Pranesh B. Aswath

Bone has the ability to heal fractures so long as the size of the fracture is sufficiently small. If the defect is large or of critical size, a filling material or graft will be needed to help bone union. Among all the available methods to address this medical condition, the common drawback of grafts is that they are limited in supply since a biological site or organism is needed to harvest the biological graft. As a new approach, researchers have been working with bioceramics and biopolymers for their use in bone tissue engineering. In this work, chitosan was modified with methacrylic anhydride. After the methacrylation process, methacrylated chitosan (MAC) was able to print a scaffold using a 3D printer (robocasting). Then, the MAC was integrated with laponite (MAC-Lp) and the printed scaffold in order to compare its properties with methacrylated gelatin (MAG) containing the laponite (MAG-Lp) scaffolds. Mechanical, dynamic mechanical and rheological properties were measured between MAC, MAC-Lp, MAG, and

MAG-Lp. We observed that the addition of laponite increased its viscosity, storage modulus, loss modulus and mechanical strength. Later, it was studied in vitro studies using MC3T3-E1 osteoblast precursor cell lines with MAC, MAC-Lp, MAG, MAG-Lp scaffolds and it was observed that MAC, MAC-Lp results in viability. Proliferation was greater than the MAG, MAG-Lp scaffolds. Finally, every scaffold was seeded for matrix deposition at 28 days and characterized with FTIR. Similarly to MAG and MAG-Lp scaffolds, the MAC and MAC-Lp scaffolds showed Amide I, III bands and additional phosphate bands. The highest ratio occurred in the MAC-Lp and MAC scaffolds. The MAC-Lp scaffolds were characterized with SEM to demonstrate fiber, and the SEM-EDS to show Ca and P atoms. The MAC-Lp scaffolds demonstrated collagen fiber, Ca and P atoms in the SEM.

CHAPTER 1

GENERAL INTRODUCTION

1.1 Bone and grafting

Bone is a hard material that constitutes the skeletal structure in humans and vertebrates and which provides structural integrity. There are 213 bones in the adult human. Each of these bones undergoes remodeling dynamically, a consequence of mechanical and biochemical processes in the body. In all vertebrates, there are two kinds of bone, cortical bone which is dense, and trabecular bone which is very soft. The human skeleton comprises approximately 80% cortical and 20% trabecular bone [2]. Bone is a complex material and it is a living tissue that has the ability to repair itself. Bone healing is divided into three stages: an inflammatory phase, a reparative phase, and a remodeling phase [3]. The presence of a critical size defect limits the ability of bone to heal and fill the defect, so the use of grafts to assist in the healing process is required. There are three types of graft used to assist in healing defects that are larger than the critical size, including autograft, allograft, [4] and xenograft [5]. An autograft is a tissue or organ which is grafted from one point to another in the same body. While the autograft is the gold standard in bone grafts as it has the best integration characteristics, it has some drawbacks such as morbidity of the donor site. An allograft is a tissue or organ from any other individual of a species as a recipient and grafted. On the other hand, in the case of the allograft, there is the possibility of infections and rejection of the graft. [4]. A xenograft is a tissue or organ from donor of a different species and transplanted to a member of another species. Xenografts have significant limitations as the grafts are not of human origin. All of these grafts have a short shelf life, which further limits their application [5]. All these drawbacks have triggered numerous studies to find a new method to heal bone defects.

Over the past 25 years, biomaterials have started to replace graft applications. These biomaterials are either natural or synthetic. Their usage is not limited to healing bone and these materials can be used to replace damaged tissue and even organs [6].

1.2 Biomaterials

Biomaterials can be polymers, ceramics, composites or metals and have been used for a long time. Polymers, particularly hydrophilic polymers, form cross linked networks. A specific example of these is hydrogels [7].

1.3 Hydrogel

Hydrogels are three-dimensional networks polymers. They are composed of hydrophilic crosslinked polymers either bonding covalently or held with physical attractions. Hydrogels can hold huge amounts of water or biological fluids inside their structures and swell without dissolving. The carboxyl, amino, amide, and hydroxyl group of hydrogels have high hydrophilicity. Hydrogels in swollen states are soft, rubbery, and to some extent, they resemble living tissue. They have been used since the 1950s and their use has increased greatly in recent times [8]. Currently, new methods to design hydrogels have been taken over by traditional chemical methods, such as freeze drying, fiber bonding and solvent casting resulting in self-assembling, such as the solid free form technique. Hydrogels are currently being used in tissue engineering and drug delivery [9]. Hydrogels have many properties similar to biological tissue, such as hydrogels providing three-dimensional structural support for cells, providing a highly hydrated, cytocompatible environment and facilitating nutrient and waste transport. These examples show how hydrogels resemble biological tissue and can be implanted or injected into the human body. Moreover, their water absorbing capacity simplifies hydrophilic molecules such as proteins and peptides within the polymeric network [10]. Requirements of biomaterials

include biodegradability, cytocompatibility, biocompatibility, protein stability, and ease of formulation. These are all characteristics in an ideal hydrogel [11].

The structure of hydrogels can vary based on the types of polymers used in their construction, such as block copolymers, branched polymers, etc. Changes in polymer design can enable the customization of hydrogel properties that include mechanical strength [12].

Polymeric hydrogels can be composed of natural or synthetic materials. Polysaccharides such as hyaluronic acid and chitin/chitosan are natural polymers [13] [14] Moreover, proteins such as collagen, gelatin, and fibrin are also natural polymers [15] [16] [17] [18]. Natural polymers have different advantages, including biocompatibility and biodegradability. On the other hand, they have many drawbacks such as difficulty to scale production, batch-to-batch variation in properties and ability to manufacture pure products. In addition, they also have lower mechanical properties compared to many other biomaterials [12]. There are some synthetic polymers such as polyethylene glycol [19], polyvinyl alcohol (PVA) [20], poly (hydroxymethymetacylate) p(HEMA) [21] and methacrylic anhydride [22] that can be used as hydrogels. In this thesis, we examined the modification of methacrylic anhydride with chitosan and gelatin after examining their physical and biological properties.

1.4 Gelatin

Gelatin is a composite of peptides and proteins that it is produced by the hydrolysis of collagen extraction. This extraction is from the skin, bones, and connective tissues of animals such as pigs, chickens and fish [23] [24]. These are acid, alkali, or enzyme treatments to break polymer fibrils into small peptides. After these processes, filtration, evaporation, grinding, sterilization, and shifting may occur [23]. Gelatin resembles collagen in terms of molecular structure [24].

Collagen and gelatin have their main structural proteins in the extra cellular matrix of connective tissues. They are being utilized as potential materials for tissue engineering, especially in the field of the replacement of damaged tissue. For instance, collagen type I exists in bone tissue. Gelatin demonstrates several advantages including suitable solubility and less antigenicity when compared to its precursor [25] [26]. In addition, signaling peptides, such as the Arg-Gly-Asp (RGD) sequence of gelatin, can promote cell adhesion, migration, differentiation and proliferation [26].

Gelatin is a network of polymer chains. This network promotes physical, ionic, or covalent interaction between polymers. Water exists in the interstitial spaces between polymeric chains. Hence, gelatin has good flexibility similar to human tissue. In addition, it is biocompatible [27] [28] [29] [30]. Although it has a number of advantages for applications in tissue engineering, a major shortcoming is its poor mechanical properties. It is very sensitive to temperature and is stable only within a small temperature range. Gelatin is a homogenous material but its drawback regarding its mechanical properties can be tailored by reinforcing it with crosslinking interpenetrating networks such as clay particles, by crystallite formation or by modifying it with other polymers [23]. Since it excellently mimics the extra cellular matrix, it is preferred for the regeneration of tissue and for temporary support of cell growth. [24] [27, 28].

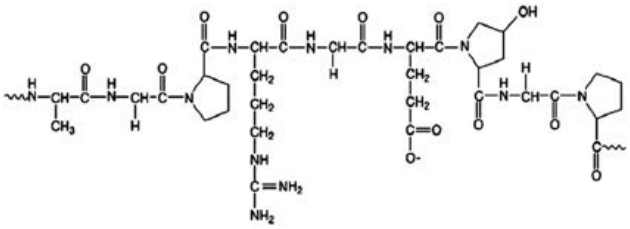

Figure 1.1 Basic chemical structure of gelatin [31]

1.5 Chitosan

Chitosan is obtained by the deacetylation of chitin [32, 33]. It is the second abundant polymer

which is extracted from the exoskeleton of shrimp, lobster, and crabs. In addition to the second abundant polymer, there are also another advantages such as low cost and easy availability [34]. Moreover, chitosan has different physicochemical characteristics such as molecular weight, crystallinity, deacetylation and positive charge. It is soluble is in weak acids (pH<6.3) and it can be easily processed into porous scaffolds [35]. It is a linear polysaccharide and a combination of a copolymer of N-acetyl glucosamine and N-glucosamine [36]. Chitosan's metabolization into non-toxic D-glucosamines comes from lysozymes and becomes biodegradable [37]. Lysozyme is a non-immunological enzyme and a well-characterized carbohydrate hydrolase [38]. It can also be turned into gels, fibers, or beads [39], and is being used for tissue engineering applications [40] [41]. Lysozyme is especially secreted by the osteoclast and is active in breaking down and rebuilding bone in bone tissue engineering. There are a number of methods to create chitosan hydrogel, such as pH or temperature changes, and the chemical crosslinking of polymers [32]. Chitosan has played a major role in bone tissue engineering over the years. It is biodegradable, biocompatible and antibacterial. There are many examples chitosan based scaffolds in the tissue engineering field for bone regeneration such as sponges [42], hydrogels [43] and composite hybrids [44]. Chitosan resembles osseous and chondral glycoproteins. The chemical structure of chitosan demonstrates that it contains many amine groups inside it and these amine groups can be used as nucleophiles to create modifiable chitosan. It occurs as a protonation between these amino groups to render chitosan hydrophilic and soluble in water [45].

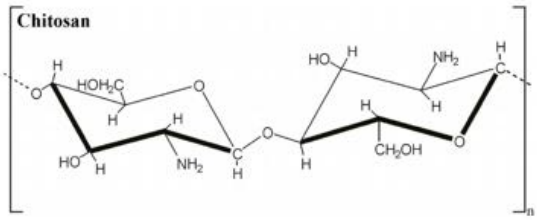

Figure 1.2 Basic chemical structure of chitosan [46]

1.6 Bioceramic

A bioceramic repairs and reconstructs the damaged tissue parts of the skeletal system. Since, it is inert (alumina-zirconia), resorbable (tricalcium phosphate), bioactive (hydroxyapatite, bioactive glass, and glass-ceramics), or porous for tissue growth (hydroxyapatite – coated metals), it has been used in the market for a long time.

The most common bioceramics are hydroxyapatite (HA) and bioglasses. Based on its chemical similarity to bone, HA is the one of them [47]. HA and bioactive glass are both osteoconductive. They facilitate cellular migration and enhance extracellular matrix (ECM) attachment to their matrices. Porous scaffolds made from these materials enhance mineralized tissue [48] [49, 50] [51] [52]. However, they have some drawbacks such as degradation and immunological issues [50]. Recently, synthetic biomaterials containing Si^{4+} have gained much attention. Previous studies [51-54] have shown that leached Si^{4+} from these materials is directly linked to the enhancement of collagen type I expression and mineralized tissue synthesis. It also plays a role in enhancing the mechanical properties of bone femurs in mice [53], suggesting that Si^{4+} may play an essential role in influencing the physical properties of the matrix. In mice, rat and chicken animal models, Si-deficiency leads to irregular bone development and weak bone formation, while the administration of elevated dietary levels of Si enhances bone growth and restores normal bone function [53] [54] [55]. Bioactive glasses are FDA approved biomaterials

containing Si^{4+}. They degrade faster than Ca-P based scaffolds and improve tissue attachment by forming a "bone-like" surface HA layer [56]. These materials, however, degrade partially and microencapsulate within the bone and possibly in the connective tissue. Newly developed mesoporous bioactive glasses do not become microencapsulated. However, in addition to difficulties in the preparation of such scaffolds, they suffer from high degradation rates due to their high surface area. The fast degradation of mesoporous bioactive glass results in premature resorption and also fast ion release, which may lead to ectopic mineralization in connective tissue [57] [58]. Adjusting degradation rate of mesoporous bioactive glass is challenging due to the lack of control of the porosity in the fabrication process [59] [60].

1.7 Laponite

Laponite is a synthetic layered silicate ceramic. It is used due to the improvement in its mechanical, dynamic mechanical and biological properties. When laponite disperses in water, it forms colloidal particles that can be used as a filler or thickening mechanism. It is a 2:1 layered smectite clay mineral which has one octahedral MgO_2 sheet sandwiched between two SiO_4 tetrahedral sheets. Its formula is $Na^{+}_{0.7}[(Si_8Mg_{5.5}Li_{0.3})O_{20}(OH)_4]^{-0.7.}$ Generally, the tetrahedral sheet is silica (SiO_4) where three O^{2-} ions in each tetrahedron are shared with the three nearest neighboring tetrahedral silica molecules, while the fourth O^{2-} ion is not shared with another tetrahedron and is free to bond [61]. Laponite (Lp) is a nanopowder which can be used as an osteogenic inducer in the matrix [62] [63] [64] [65].

By releasing $Si(OH)_4$, it acts as a bioactive glass and enhances osteogenesis.

Lp reacts with water as in liquid media:

$Na^{+0.7}[(Si8Mg5.5Li0.3)O20(OH)4]^{-0.7} + 12H^{+} + 8H2O \rightarrow$

$0.7Na^{+} + 8Si(OH)4 + 5.5Mg^{2+} + 0.3Li^{+}$

It is known that this reaction increases alkalinity. This increment occurs by consuming H^{+}. Another important parameter is the leaching of Na^{+}, Mg^{2+}, and Li^{+} ions into the water that shows that laponite may react with water.

Magnesium ions facilitate cell adhesion through adhesion proteins of the integrin family. Lithium ions enhance osteogenesis by increasing the RUNX2 expression. Li^{+} enhances Wnt-associated gene expressions that inhibit beta-glycogen synthase kinase-3, which in turn regulates RUNX2 activity [65].

Laponite has a special shape with two charges in the body. Since it is nano-disc shaped, it has thickness and diameter. The thickness is 1 nm and the diameter is approximately 20 nm. This unique shape is crucial for application. The shape gives the particles a high surface-to-volume ratio. Due to dissociation of of Na^{+} from the surface, Lp nano-discs gain negative charges. Even though the surface has positive charge, the edges are negatively charged and due to this partial charge, an electrostatic interaction occurs between the surface and edges [66].

It is well known that laponite can be used as a thickening agent which leads to a thick thixotropic gel in addition laponite leading to hydrogel. Therefore, laponite increases the viscosity of hydrogel. It can be entangled with a biopolymer to create a rigid structure.

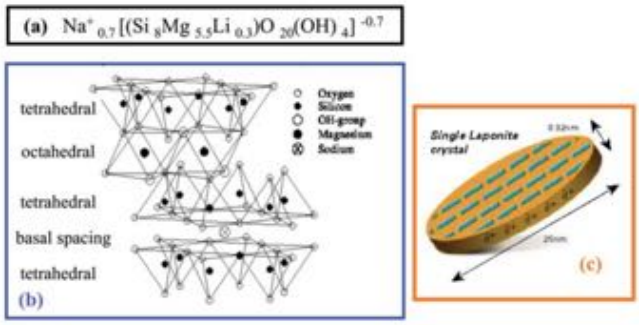

Figure 1.3 (a) Empirical formula of laponite, and (b) Idealized structural formula of Laponite, and (c) Single Laponite platelet [67]

1.8 Crosslinking Mechanism

Crosslinking is very significant process for polymer interaction. It is a bond that can be linked from one polymer to another polymer. Bonds can be covalent or ionic. This term, when used in the biological field, refers to creating networks between polymers for polymer-polymer interaction. The aim of crosslinking is to protect hydrogels from dissolution in liquid media. The mechanism can be either physical or chemical [68]. Physical crosslinking relies on nonreversible bonds in a hydrophobic interaction. However, the most negative side of physical crosslinking is stability. Its stability is limited such that mechanical strength and stability decrease in time. The new method is chemical crosslinking. The mechanism of chemical crosslinking is to bond covalently. Radical polymerization is one of the many methods to accomplish crosslinks chemically [10] [69] In this thesis, radical polymerization was utilized with an existing IRGACURE 2959 radical photoinitiator for the UV curing of systems with unsaturated monomers and prepolymers. The chemical formula of IRGACURE 2959 is (2-Hydroxy-1-[4-(2-hydroxyethoxy) phenyl]-2-methyl-1-propanone). It is especially utilized in water-polymer systems based on acrylate or unsaturated polyester resins. The active hydroxyl group can be reacted with suitable functionalized unsaturated resins [70].

.

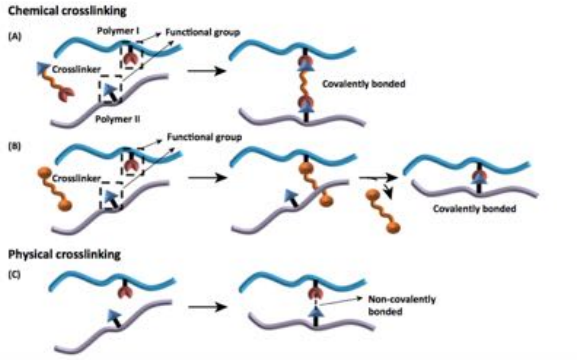

Figure 1.4 Schematic of the three methods of crosslinking (a) Chemical crosslinking with the crosslinker incorporated into the bond (b) Chemical crosslinking with the crosslinker not incorporated into the bond (c) Physical crosslinking [71]

1.9 Photopolymerization

Photopolymerization is a type of radical polymerization. It allows the formation of chemical crosslinking between (meth)acrylate ((M)AA) and polymer chains. It is initiated by a photoiniator. The photoiniator decomposes and generates radicals responding to UV or visible light. A number of photoiniators are available in biomedical applications. The most widely used is IRGACURE 2959. It is efficient and biocompatible at low dosages. This technique is suitable for in situ gel formation [72]. Due to the photoiniator, photocuring occurs. This curing system is fast and can be done at room temperature without use of chemicals. Due to this photocuring [21], this polymerization technique applies for chemical and physical crosslinking to biodegradable polymers that can be used in tissue engineering. In the photocrosslink system, hydrogel formation occurs rapidly under visible or UV light by helping the photoiniator [73].

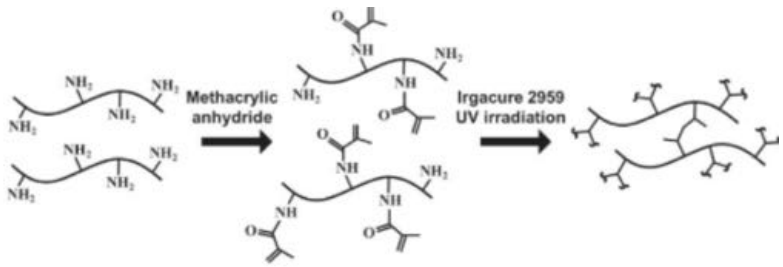

Figure 1.5 Photo crosslinking process of MAG [74]

1.10 Applications of Hydrogel

1.10.1 Tissue Engineering

Tissue engineering started to be active 20 years ago. Since the need for donor organs and tissues has been increasing year by year, this field has been opened to new solutions. Based on statistics, approximately 1 million dental bone graftings were performed in the United States in 2006, and the number has been significantly growing annually at a rate of 15% [75].

The basic principle of tissue engineering is to regenerate and remodel an organ or tissue utilizing three-dimensional matrices. These three-dimensional matrices are called scaffolds.

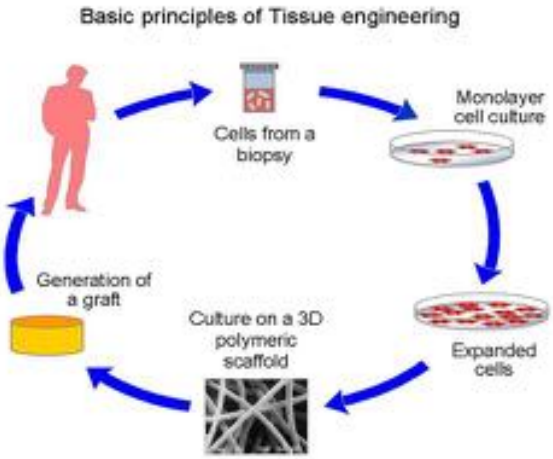

Figure 1.6 Schematic of the basic principles of tissue engineering by using hydrogels as extracellular matrix [70]

Scaffolds fundamentally act as templates for tissue and they can be seeded with cells with or without a growth factor. They apply different types of mechanical and chemical stimuli to cells. These cell cultured scaffolds enhance the synthesize tissue. Then it may be implanted into an injured site to regenerate tissue induced in vivo. There are a number of techniques to fabricate scaffolds such as molding, freeze drying, fiber bonding or printing [76] [77] [78].

The use of polymers (synthetic, natural or combinations thereof) to prepare hydrogels offers a functionalized and different chemistry using a peptide sequence to improve interactions with cells. Most of hydrogels derivative with adhesive peptides, such as RGD sequence or glycoprotein to promote cells [79].

1.11 Additive Manufacturing – Robocasting

The architecture of a material is one of the crucial criteria in tissue engineering applications. There are a number of conventional methods on the market. These include phase separation, fiber bonding, freeze drying, solvent casting and the melt based method. However, they are time consuming, labor-intensive and do not provide exact control over the architecture. Unlike the traditional methods, computer-controlled microfabrication processes have been developed to fabricate scaffolds with complex shapes and predesigned architectures. In Solid free form (SFF) fabrication, which is one of the novel scaffold fabrication techniques, each scaffold is formed by selectively adding the material layer by layer, under the control of a computer. The new methods have many advantages. Predictable porosity and complex shapes are two of advantages of this technique. One of these methods is rapid prototyping. This is a technique was a revolution in the fabrication industry.

Rapid prototyping has two branches: additive and subtractive. Additive rapid prototyping (ARP) is more popular than the subtractive rapid prototyping in the market. Due to fact that ARP allows creation of more complex shapes and hollow structures, it is more desirable [80]. The broad category of ARP includes stereolithography, fused deposition modeling, direct metal laser sintering, laminated object manufacturing, electron beam melting, selective laser sintering, laser engineered net shaping and three-dimensional (3D) printing. 3D does not require heat for its functionality, which makes it useful for cell or growth factor incorporation [81].

Robocasting, or direct ink writing (DIW), is a sub-branch of three-dimension printing which is based on a computer aided fabrication method. In this method, the extrusion of the ink is utilized to move in all three axes to create two-dimension layers By adding layer on layer, a three-dimensional object is created. The robocaster allows precise control of micropatterning by determining the dimensions of filaments, the size and shape of pores and the percentage of porosity of the scaffold [82] [83]. Although extensive research has been conducted on suitable biomaterials for 3DP, there are few well-stablished biomaterials on the market that can be 3D printed and implanted into the body [84]. These materials include bioceramics such as bioglass, TCP and HA, and biopolymers such as PLLA, PGA and PLGA.

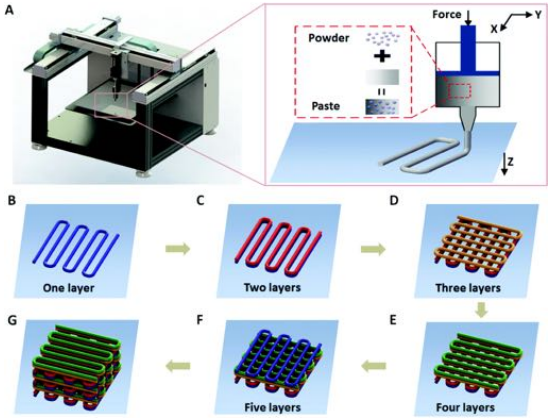

Figure 1.7 Schematic diagram of a scaffold prepared using the layer-by-layer 3D robocasting technique. (a) The 3D robocasting machine. Inside is drawing of the extrusion equipment (b-g) The schematic diagram of the printing process of the scaffold [85]

1.12 Aim of thesis

The first aim of this thesis is to investigate the potential use of a novel biodegradable hydrogel, based on methacrylated chitosan to create scaffolds. Later, it is integrated with laponite as a controlled synthetic extracellular matrix that can facilitate osteoblast mineral formation. In this work, the three-dimensional scaffolds made from methacrylated chitosan-laponite reveal a visco-elastic network that can be stabilized by chemical cross-linking via photopolymerization. This approach is the first of its kind and it stands out to be a promising candidate for bone tissue engineering as it provides benefits such as cell growth and matrix deposition.

Aim 1: Synthesis of methacrylated gelatin and methacrylated chitosan and their integration with laponite.

1.1 Synthesizing methacrylated gelatin

1.2 Synthesizing methacrylated chitosan

Aim 2: Three-dimensional scaffold printing using photopolymerization.

2.1 Injectability evaluation

2.2 Scaffold composition and ink preparation

2.3 Adjusting material and printing parameters

2.4 Determination of UV intensity

Aim 3: Material characterization and in-vitro studies.

3.1 Confirmation of methacrylation process with FTIR method.

3.2 Measurement of viscosity and rheological properties

3.3 Measurement of the compressive strength

3.4 Surface quality with SEM, and stereo microscope.

3.5 Studying cell attachment, viability, proliferation, and matrix deposition with MTS Assay and Confocal Microscope

3.6 Confirmation in vitro studies with FTIR, Raman, and SEM-EDS

CHAPTER 2

PAPER 1

3D PRINTED BASED NANOSILICATE SCAFFOLD ENHANCE OSTEOGENIC DIFFERENTIATION

Tugba Cebe,[a] Felipe Monte,[b] Neelam Ahuja,[c] Siddiqui Danyal,[d] Danieli Rodrigues [d], Pranesh B. Aswath,[a] Venu G. Varanasi,[c*]

[a] Department of Materials Science and Engineering, University of Texas at Arlington, Arlington Texas 76019, USA

[b] Department of Bioengineering, University of Texas at Arlington, Arlington Texas 76019, USA

[c] Department of Biomedical Sciences, Texas A&M University College of Dentistry, Dallas, Texas 75246, USA

[d] Department of Bioengineering, University of Texas at Dallas, 800 W. Campbell Road Richardson, TX 75080-302, USA

* To whom correspondence should be addressed:

Venu G. Varanasi, Ph.D.

3302 Gaston Avenue, Texas A&M Health Science Center, Dallas, Texas 75246, USA

Phone: +1-214-370-7006

Fax: +1-214-874-4538

E-mail: vvaranasi@tamhsc.edu

1. Abstract

Bone has the ability to heal fractures so long as the size of the fracture is sufficiently small. If the defect is large or of critical size, a filling material or graft will be needed to help bone union. Among all the available methods to address this medical condition, the common drawback of grafts is that they are limited in supply since a biological site or organism is needed to harvest the biological graft. As a new approach, researchers have been working with bioceramics and biopolymers for their use in bone tissue engineering. In this work, chitosan was modified with methacrylic anhydride. After the methacrylation process, methacrylated chitosan (MAC) was able to print a scaffold using a 3D printer (robocasting). Then, the MAC was integrated with laponite (MAC-Lp) and the printed scaffold in order to compare its properties with methacrylated gelatin (MAG) containing the laponite (MAG-Lp) scaffolds. Mechanical, dynamic mechanical and rheological properties were measured between MAC, MAC-Lp, MAG, and MAG-Lp. We observed that the addition of laponite increased its viscosity, storage modulus, loss modulus and mechanical strength. Later, it was studied in vitro studies using MC3T3-E1 osteoblast precursor cell lines with MAC, MAC-Lp, MAG, MAG-Lp scaffolds and it was observed that MAC, MAC-Lp results in viability. Proliferation was greater than the MAG, MAG-Lp scaffolds. Finally, every scaffold was seeded for matrix deposition at 28 days and characterized with FTIR. Similarly to MAG and MAG-Lp scaffolds, the MAC and MAC-Lp scaffolds showed Amide I, III bands and additional phosphate bands. The highest ratio occurred in the MAC-Lp and MAC scaffolds. The MAC-Lp scaffolds were characterized with SEM to demonstrate fiber, and the SEM-EDS to show Ca and P atoms. The MAC-Lp scaffolds demonstrated collagen fiber, Ca and P atoms in the SEM.

2. Introduction

Bone is calcified tissue and it is a complex material as well as living tissue. It supports structural mechanisms, and it provides protection, mineral storage and pH regulation. Even if bone is assumed to be static, it is a living material that needs to renew itself [86].

Bone remodeling needs the coordination of cellular, hormonal and molecular systems [42]. In the cases of defects, bone can heal itself so long as the size of the defect is sufficiently small. If the defect is large or critical in size, a filling material or graft will be needed to help bone union. 'Critical size' means that the bone is beyond the ability of natural repair, which results in loss of function. Such defects can result from trauma, surgery or degenerative disorders [87].

In spite of a number of traditional treatments such as artificial implants, joint replacements, their performance is limited. Therefore, grafts are not necessarily the solution to the problem [51] [88]. In recent years, three-dimensional (3D) hydrogels have appeared in the market as new approaches [89]. The function of scaffolds influences seeded cells. Regeneration of bone may occur by means of functioning extra cellular matrices (ECM), support surface contact, temporarily mechanical structure or maintaining space [44]. The requirements of scaffolds include biocompatibility, porosity, good surface chemistry for cell attachment, proliferation and differentiation [90]. The mechanical properties, swelling, and degradation behavior play significant roles in adhesion, growth and regeneration [91] [92, 93]. In this study, two natural biopolymers, namely gelatin and chitosan, were utilized. Chitosan is a derivative from chitin and conducive to osteoblasts [41]. Gelatin is a derivative from collagen and collagen is a major component of the ECM of bone [94]. Both enhance viability, proliferation and differentiation of osteoblast-like cells. Since their mechanical properties need to improve, a methacrylation process has been achieved with two groups. A clay mineral, laponite, was employed to increase the

mechanical, dynamic mechanical and rheological properties of chitosan and gelatin to support osteogenic mineral formation. It was designated to ability of the composite 3D hydrogel scaffolds to support osteogenic mineral formation, and the effects on their mechanical strength and swelling.

3. MATERIALS AND METHOD

3.1 Methacrylated Gelatin Synthesis

Dulbecco's phosphate buffered saline or DPBS (21-031-CV CORNING cellgro) was heated to 60°C. 0.1 g/mL of powdered gelatin from porcine skin with a Bloom Index of 300 (G1890 Sigma) was mixed and allowed to dissolve the gelatin completely [95]. The dissolution time was 20 mins after which the temperature was reduced to 50°C and 0.77 mL of methacryclic anhydride (MA) (276685 SIGMA ALDRICH) per gram of gelatin was added to the solution at a stirring rate of 12 mL/h using a syringe pump (COLE PARMER, VERNON HILLS, ILLINOIS). After adding the MA, the solution was stirred for 3 hours. Figure 3.1 illustrates the methacrylation reaction.

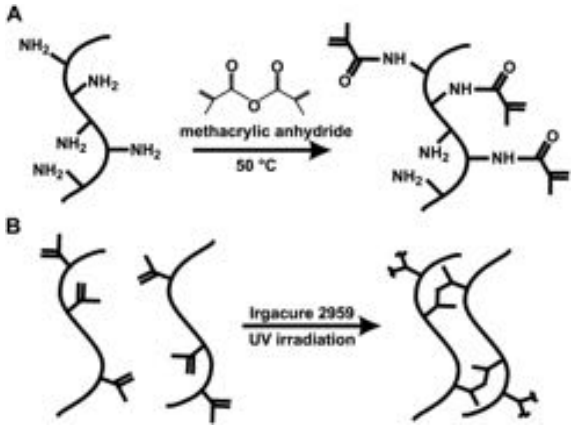

Figure 3.1 Synthesis of methacrylated gelatin. (a) Gelatin macromers containing primary amine groups were reacted with methacrylic anhydride (MA). (b) To create a hydrogel network, the methacrylated gelatin was crosslinked using UV irradiation in the presence of a photoinitiator

[95].

Later, the solution was transferred to a 12-14 kDa dialysis tube (Spectra/Por® 4, Dialysis Membranes, MWCO 12000 to 14000, Spectrum® Laboratories INC) and dialyzed against DI water. The system was continuously stirred for one week at 40°C to filter the methacrylic acid and any unwanted reagents. The water was changed every day to maintain osmotic pressure in the system. After dialysis, the solution was transferred to petri dishes and the temperature lowered to –80°C to freeze for one day. The purified solution was transferred to a freeze-dryer (LABCONCO FreeZone 2.5) and lyophilized for 1 week to isolate the MAG [95].

After synthesis of each batch, the samples were analyzed by FTIR (Thermo SCIENTIFIC NICOLET iS10 SMART iTR) to confirm successful methacrylation.

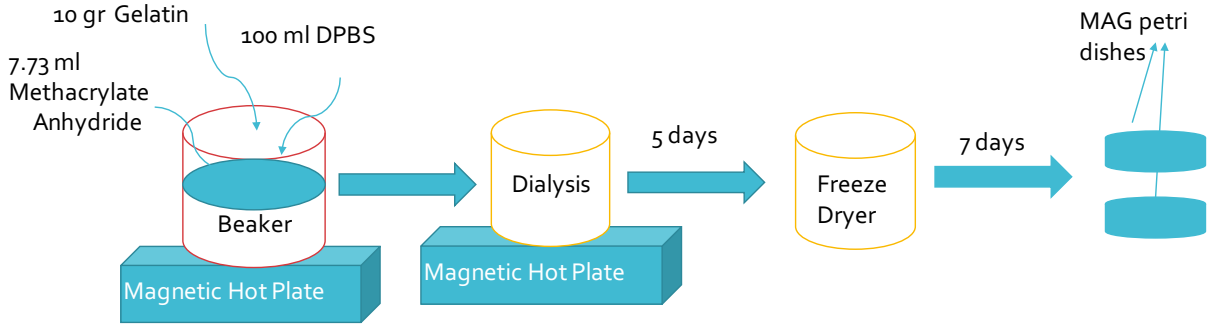

Figure 3.2 Schematic illustration of methacrylated gelatin synthesis

3.2 Methacrylated Chitosan Synthesis

Methacrylated chitosan was synthesized according to the literature with minor modifications [96].

First, chitosan was bindered to reduce particle size (KRUPS F203), after which a dried sample was weighed and dissolved in 25 mL of 2.8% acetic acid; then 25 mL of ethanol was poured into

the solution. Later, the methacrylic anhydride (chitosan to MA molar ratio 0.5 M) was charged speeding at 12 mL/h with a syringe pump (COLE PARMER, VERNON HILLS, ILLINOIS). It was stirred at an ambient temperature for a determined time. All this process was achieved by using a mechanical stirrer (RW 20, IKA).

Later, the solution was transferred to a 12-14 kDa dialysis tube (Spectra/Por® 4, Dialysis Membranes, MWCO 12000 to 14000, Spectrum® Laboratories INC) and dialyzed against DI water. The system was continuously stirred for one week at 40ºC to filter the methacrylic acid and any unwanted reagents. The water was changed twice per day to maintain osmotic pressure in the system. After dialysis, the solution was transferred to petri dishes and put into freezing at –80ºC for one day. The purified solution was transferred to a freeze-dryer (LABCONCO FreeZone 2.5) and lyophilized for 1 week to isolate it.

After synthesis of each batch, the samples were analyzed by FTIR (Thermo SCIENTIFIC NICOLET iS10 SMART iTR) to confirm successful methacrylation.

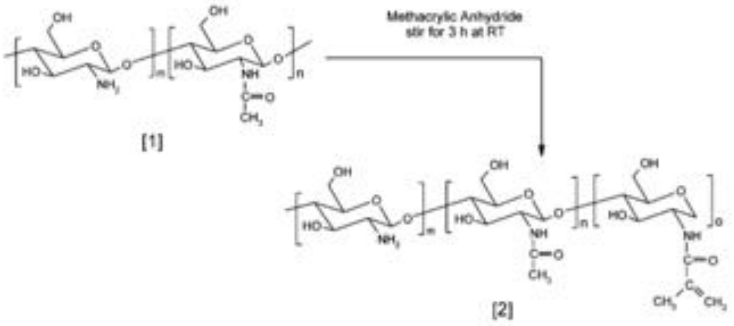

Figure 3.3 Chitosan [1] primary amine groups react with methacrylic anhydride to produce methacrylamide chitosan (MAC) [2]. Free radical polymerization of MAC on the methacrylamide group [97].

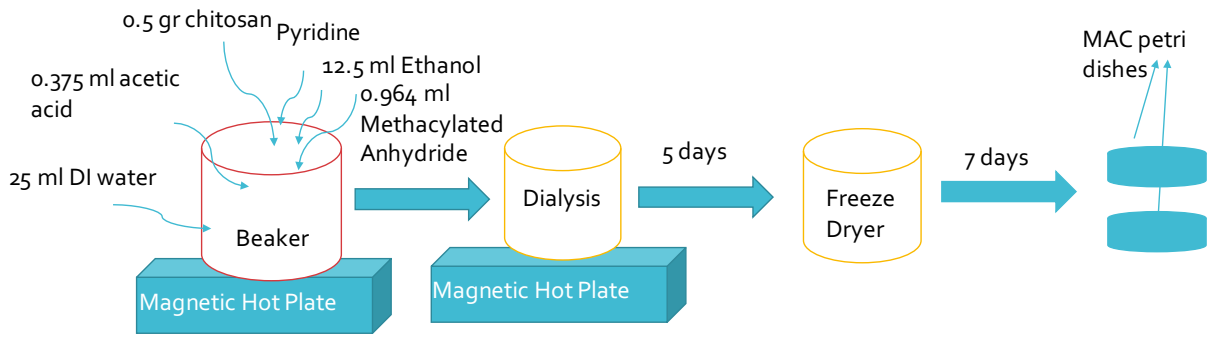

Figure 3.4 Schematic illustration of methacrylated chitosan synthesis

3.3 Injectability Evaluation

Injectability means that paste can be extruded to from a syringe, ideally in a homogenous manner under an applied force [98]. Injectability is directly related to the viscosity of the hydrogel. In addition, a number of factors lead to different conditions such as temperature and time. A homogenous paste for all four groups was a benefit for the extrusion force. If the paste were to be more viscous, it would increase the extrusion load and possibly clog the top of the syringe, thereby preventing printing. If the paste were more liquid, it would have decreased the load and effects of the shape of the scaffold [99] [100].

The injection was regulated by applying 80°C to the MAG, MAG-Lp, and MAC-Lp inks. Since the mass fraction was lower in the MAC inks, heating to 80°C decreased the viscosity more, and it was not able to print. A temperature of 65°C was selected for the MAC scaffold. Finally, the rheological properties of the inks of all four group were measured with a rheometer (RH 3, TA instruments University of Texas at Dallas).

3.4 Scaffold Composition and Ink Preparation

Since it has four groups all of was different preparation even though they have common parts.

3.4.1 Methacrylated Gelatin

To determine prepare ink with freeze dried MAG, MAG-Lp, they were prepared based on the previous study [95]. The temperatures of the MAG-Lp, MAC, and MAC-Lp were determined based on the MAG procedure. DPBS was mixed with 0.8% (w/v) 2-hydroxy-1(4-(hydroxyethoxy) pheny)-2-methyl-1-propanone (Irgacure 2959) at 80ºC until completely dissolved. The solution was stirred for 3 minutes. Afterward, a pre-weighted MAG was added to the solution and transferred to a Planetary Centrifugal Mixer (THINKY ARE-310) and mixed for 15 minutes at 2000 rpm. Figure 2.3 shows a schematic process of ink preparation at the micro scale. After mixing, the nanocomposite was transferred to a 3 cc UV protected dispenser tube (Nordson EFD Optimum® Light Block AmberBarrels), sealed and centrifuged for a half minute at 2.2 krpm to remove all the air trapped inside the ink. This is a very crucial step; if the syringe is not properly de-bubbled, the continuous material injection in the robocaster will be interrupted, the filament will rupture and the entire scaffold will distort.

3.4.2 Methacrylated Gelatin and Laponite

Every process was the same as the preparation of the MAG. The difference between the preparation of MAG and MAG-Laponite was the addition of laponite and sucrose as well as the mixing times and speeds. After adding the Irgacure 2959, 4% sucrose and 4% laponite were added to the DPBS at 80°C.

After mixing, the nanocomposite was transferred to a 3 cc UV protected dispenser tube (Nordson EFD Optimum® Light Block AmberBarrels), sealed and centrifuged for 1 minute at 4.4 krpm to remove all the air trapped inside the ink.

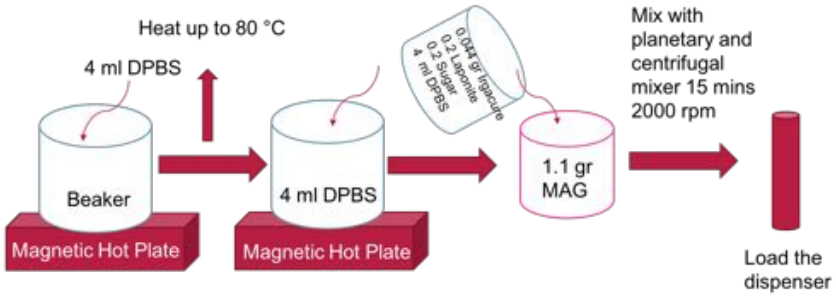

Figure 3.5 Schematic illustration of MAG-Lp ink preparation

3.4.3 Methacrylated Chitosan

The MAC mass fraction was 10% in the hydrogel. 0.8% w/w (MAC) I2959 was added to pre-heated DPBS (at 65ºC) and mixed. The solution was stirred at 65ºC for 3 minutes. Afterward, a pre-weighted MAC (10%) was transferred to a mixer container and 2% acetic acid was added to increase dissolution. Later, the solution was mixed with MAC and transferred to a Planetary Centrifugal Mixer (THINKY ARE-310) and mixed for 30 minutes at 2000 rpm.

After mixing, the nanocomposite was transferred to a 3 cc UV protected dispenser tube (Nordson EFD Optimum® Light Block AmberBarrels), sealed and centrifuged for 1 minute at 4.4 krpm to remove all the air trapped inside the ink.

3.4.4 Methacrylated Chitosan and Laponite

Every process was the same as the preparation of MAC. The difference between the preparations of MAC and MAC-Lp was the addition of laponite, sucrose as well as mixing time and speed. After adding Irgacure 2959, 4% sucrose and 4% laponite were added.

After mixing, the nanocomposite was transferred to a 3 cc UV protected dispenser tube (Nordson EFD Optimum® Light Block Amber Barrels), sealed and centrifuged for 1 minute at 4.4 krpm to remove all the air trapped inside the ink.

.

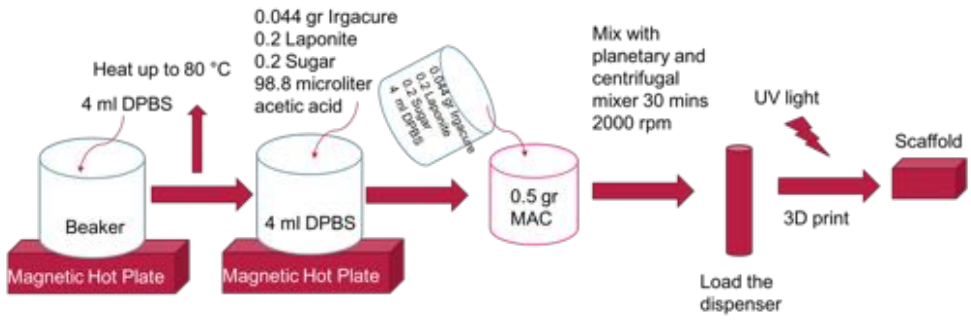

Figure 3.6 Schematic illustration of MAC-Lp ink preparation

Composition	Temperature	Stirring Time	Mixing Time	Mixing Speed
MAG	**80 °c**	**3 mins**	**15 mins**	**2000 rpm**
MAG- Lp	**80 °c**	**3 mins**	**15 mins**	**2000 rpm**
MAC	**65 °c**	**3 mins**	**30 mins**	**2000 rpm**
MAC – Lp	**80 °c**	**3 mins**	**30 mins**	**2000 rpm**

Table 3.1 Schematic diagram of temperature, time, and speed for MAG, MAG-Lp, MAC, MAC-Lp scaffolds

Composition	Debubbling time	Debubbling speed
MAG	**30 sec**	**2.2 krpm**
MAG- Lp	**1 min**	**4.4 krpm**
MAC	**1 min**	**4.4 krpm**
MAC – Lp	**1 min**	**4.4 krpm**

Table 3.2 Schematic diagram of debubbling time, and speed for for MAG, MAG-Lp, MAC, MAC-Lp scaffolds

3.5 Rheological and Dynamic Mechanical Properties

Flow behavior of hydrogel is given by the relationship between the shear stress τ and the shear rate $\dot{\gamma}$. Changing in the shear strain per unit time gives the rate. In the meantime, shear stress is the slope of the force which is applied per unit area. The ratio of stress to rate defines viscosity η:

$\eta = \frac{\tau}{\gamma}$ Equation 3

where τ = shear stress and γ = shear rate

Similarly, to the elastic modulus, viscosity η is a measure of the resistance of the fluid to shear flow. There exist Newtonian and non-Newtonian fluids. Pseudoplastic fluids are a subset of non-Newtonian fluids and they show shear thinning behavior. Clay suspensions that contain polymers can be characterized by this behavior method. This means that when the shear rate is increased, the viscosity decreases. This can be explained by breaking down of the flocks in the colloidal systems [101].

Another fundamental property is dynamic mechanical behavior. These analyses provide information on the gel strength expressed as viscosity or elasticity and the relation of this strength to the gel composition and its stability [102].

Rheological properties of the MAG, MAG-Lp, MAC, and MAC-Lp tests were measured at the Bioengineering Department, University of Texas at Dallas. Dynamic shear oscillation measurements at small strains were used to characterize the viscoelastic properties of cross-linked methacrylamide modified gelatin and chitosan hydrogels. These rheological measurements of oscillatory shear deformations were measured with the HR 3 rheometer (TA Instruments, University of Texas at Dallas) using cone plates 40 mm in diameter and a plate-to-plate distance of 600 μm for MAG and MAG-Lp, and 400 μm for MAC and MAC-Lp to perform frequency sweep experiments (0.01–1000 rad s^{-1} with a strain of 5%) to collect storage (G') and loss (G'') moduli.

3.6 Adjusting Printing Setting

As mentioned previously, printing needs modified ink and printing settings. These settings can

be compatible for printing conditions. For example, printing speed, extrusion speed, gelatin, trapped air inside the ink, rod-to-rod distance, *z*-distance from the substrate from the starting point and the *z*-distances for each printed layer. Some of these factors are related to each other. Therefore, changing one of these factors will definitely affect another factor. For example, extrusion speed and printing speed have a direct relation to each other; an increase in extrusion speed requires an increase in printing speed to prevent filament distortion. As mentioned above, time and temperature are also two factors. The temperature will reduce gelation and viscosity of the ink.

The filament diameter should be also sufficiently thin to make it possible to produce more pores in a unit of volume. Too thin a filament will distort the scaffold integrity. A dispenser with a 0.25-millimeter inner diameter was selected for this purpose. Moreover, the *z*-distance for each printed layer was determined to be 0.196 mm. The number of layers for all four groups was determined to be 5. The three-dimensional printing device was fabricated University of Oklahoma. The software system was RoboCAD.

In this project, robocasting is one of the 3D printing methods being used. In this method, the force occurs as a plunger movement in the *z*-direction. This movement defines the extrusion speed [103].

The printing speed should be adjusted according to the "filament extrusion speed." A printing speed that is slower than the filament extrusion speed will result in accumulation and distortion of extruded filament, and a faster printing speed will result in overstretching and tearing of the filament. Table A suiTable speed for the four groups was determined to be 6 mm/min.

One of the challenges when using gelatin and chitosan hydrogel scaffolds is make them last after

fabrication. In particular, gelatin is not a self-supporting material as its micro patterning remains intact after fabrication [104]. MAG has 79.2%, MAG-Lp has 71.2%, MAC has 89.2 % and MAC-Lp has 81.2% water percentage in their respective structures. Due to their high percentage of water, 3D scaffolds do not maintain their original architecture [105]. Their tendency is to shrink in the air and swell in humid environments [106].

3.7 Minimum UV Intensity for Ink Crosslinking

The crosslinking process starts with UV light and the degree of crosslinking is related to the UV light intensity [107]. To determine the UV light intensity, scaffolds of dimensions 9 mm × 6 mm × 2 mm were printed. While printing, UV light was applied. This was called in-situ [108]. To apply the in-situ method, injected material was exposed to a UV spotlight at the tip of the printer's nozzle (THORLAB CS2010) and the light was rotated during the printing process. The complete duration for this process was 80 seconds for all four groups. Two groups, namely MAG-Lp and MAC-Lp, were designated for the dissolution test and each group was exposed to 10, 20, 30, and 40 mW/cm^2 after which we waited 28 days. After printing, the samples were filled with 2 ml α- MEM (Gibco by Life Technologies™) and incubated at 37ºC in the incubator for 28 days. During incubation, the scaffolds were monitored for any signs of dissolution. The dissolution rate of ink is directly related to the degree of cross-linkage.

The crosslinking test demonstrates that UV intensity increases, and the scaffold holds its integrity for a long time.

3.8 Swelling Test

Hydrogels have the tendency to absorb water and proteins. In general, they tend to absorb any polar solvent or solute [83]. As a result of this absorption, they swell in humid environments and

release moisture in a dry environment. This phenomenon changes the shape of the scaffold and causes swelling and shrinkage, respectively. Biological environments are wet environments and can cause hydrogel scaffolds to swell. Therefore, studying the swelling rate of ink exposed to wet environments is necessary.

Scaffolds of dimensions of 9 mm × 6 mm × 2 mm were printed and weighed subsequently (Wd). Later, they were immersed in DPBS (Dulbecco Phosphate Buffer Solution) (pH 7) at 37ºC for 1 day. Afterwards, the scaffolds were removed from the medium, their surface dried by a filter paper, and they were weighed again (Ww). The percentage swelling was calculated using the following equation:

$$\% \, Swelling = \frac{Ww - Wd}{Wd} \times 100 \quad \text{Equation 1}$$

3.9 Mechanical Test

Consideration of mechanical properties is essential to the design of nanocomposite materials. Mechanical strength is crucial to the design of materials surfaces and interfaces since they support cell growth and interact with cells to respond to inducing and maintaining strength [107]. The compressive strength of the material is related to stress and strain. There is a linear region where the material follows Hooke's Law.

$$\sigma = E\varepsilon \quad \text{Equation 2}$$

where E this time refers to Young's Modulus for compression [109]. Compressive strength is the capacity of a material or structure to bear loads tending to reduce size. The testing model is the Instron 5567 and the analyzing software was Blue Hill. Samples were prepared as 7 mm × 14 mm discs and all regulations followed the ASTM C 1424 standard. 1.00 mm/min speed and a strain rate of 20% until fracture at their compressive strength limit and the maximum

force was measured as the compressive strength. The test was a displacement measurement. It was designated to apply equal compression stress regarding the MAG, MAC groups and MAG-Lp and MAC-Lp groups. Mechanical and chemical properties are two major criteria. The same mechanical strength gives better chemical properties in comparison.

3.10 Scaffold Surface Analysis

Scanning electron microscopy (SEM) is a microscopy technique that uses a high voltage electron beam instead of an electromagnetic wave to detect objects. An SEM scans an object with a focused beam of electrons and produces images. When electrons hit the sample, they either reflect or scatter. Moreover, they can push out an electron from an atom in the sample. By collecting these electrons using a different detector, different information about specimens can be generated, including surface topography and surface chemistry. Energy-dispersive X-ray spectroscopy (EDS) is another detection technique that is usually available in SEM microscopes. When electrons from an SEM's electron gun hit the target atom and if the electron energy is sufficiently high, it can push out an electron from the inner shells and create an "electron hole." The electron hole will be filled by an electron from a higher shell which has higher energy. This difference in energy will generate a characteristic X-ray that is unique to that element. By collecting these X-ray beams, the element at the radiated point can be detected. Mapping the element distribution on the surface is also possible by using a scanning electron beam [110].

The morphology of scaffolds was first observed using the Large Fields Fluorescence Stereo Zoom Microscope (Axio Zoom.V16, ZEISS, US). Images were captured in 7×, 25×, 63×, 80×, and 125× views, after which the desired samples were prepared with the sputtering systems: CrC-100 was available for coating the conductive silver layers on the non-conductive samples

for SEM observation, and analysis by the Hitachi S-3000N Variable Pressure SEM at 20 kV and 25 kV voltage environments. Both morphology and spectra were observed using EDS.

3.11 Control Media Preparation and Cell Culture

The control media were (α - MEM; 10% fetal bovine serum, FBS and 1% penicillin-streptomycin, pen-strep). Additional supplementation of ascorbic acid (50 mg/L) (Sigma Inc, St Louis, Mo) was used in treatments for differentiation studies. Osteoblasts (MC3T3-E1 subclone 4, ATCC, Manassas, VA, passages 28-30) were cultured in 150 cm^2 flasks. Once confluent, the cells were enzymatically dissociated with 3 mL of trypsin to detach the cells and with 3 mL of α-MEM to neutralize the trypsin for the experiments. The cells were pelleted and counted (using a standard hemocytometer and inverted optical light microscope). The cells were then seeded (50,000 cells/cm^2) into 24-well plates and cultured for 1, 3 and 7 days during osteoblast mineral formation. The number of samples was three (n=6).

3.11.1 Cell Attachment

A key characteristic of an ideal scaffold is to enhance the attachment and morphology of cells. For this study, scaffolds with dimensions of 6 mm×9 mm×2 mm were printed. On each scaffold, approximately 50,000 cells per cm^2 were seeded with MC3T3 on 3D-printed scaffolds and a culture for 12 hours in a medium with 0.1% FBS. The cells were fixed in 4% paraformaldehyde and stained with Alexa Fluor® 488 phalloidin (actin) and DAPI (nuclei). Large Fields Fluorescence Stereo Zoom Microscope (Axio Zoom.V16, ZEISS, US). Images were captured in 7× to 125× views.

3.11.2 Cell Viability

Cell viability media (α - MEM; 0.1% fetal bovine serum, FBS; and 1% penicillin-streptomycin, pen-strep) were used for testing cell viability for 1 day. The measurement of cell density was performed using the MTS assay (Promega Inc., Madison, Wisconsin). This assay is colorimetric and the intensity and color were measured using a spectrophotometer (490 nm, SpectraMax Plus, Molecular Devices, San Jose, Calif.). The Kruskal-Wallis one-way Analysis of Variance on Ranks with Tukey correction was performed ($P<0.05$).

3.11.3 Cell Proliferation

Cells were treated for 7 days in each treatment (no AA) for proliferation studies. Well plates were arranged and their media were changed every 2 days. Measurements of cell density were performed using the MTS assay (Promega Inc, Madison, Wisconsin). This assay is colorimetric and the intensity and hue were measured using a spectrophotometer (490 nm, SpectraMax Plus, Molecular Devices, San Jose, Calif.). All treatments were administered in 4. The complete experiment was also repeated for statistical robustness. A Kruskal-Wallis one-way Analysis of Variance on Ranks with Tukey correction was performed ($P<0.05$).

3.11.4 Extra Cellular Matrix - Collagen Fiber

Collagen type I is the most abundant protein in the extracellular matrix (ECM), and it is the most abundant protein in the human body, accounting for 90% of bone matrix protein content [36]. Collagens are present in the ECM as fiber-liked proteins and give structural support to bone cells [43]. Samples were seeded and treated for 28 days with an ascorbic acid medium to induce cell differentiation. The scaffolds were then collected then treated with the fixation assay. After culture, samples were removed from culture, washed in DPBS twice, transferred to a fresh well plate, and fixed using 2.5% formalin (60 min), and dried using sequential alcohol dehydration

25%>50%>70%>90% and 100% ethanol–water for 5 min per concentration. Samples were dry overnight then some of them stored in fresh well plates before FTIR, Raman analyzing, the others sputtered with silver and stored in fresh well plates prior to examination by Hitachi S-3000N Variable Pressure SEM. All groups were examined with FTIR technique. MAC-Lp scaffolds were analyzed with Raman, and SEM-EDS technique.

3.12 Fourier Transform Infrared Spectroscopy for Osteoblast Formation

FTIR is a chemical analysis method based on energy absorption of covalent bonds in a sample. IR radiation excites covalent bonds from a lower vibrational energy to a higher one. This energy can be in the form of vibrational bending, rotating, wagging, stretching, twisting, etc. Each covalent bond can absorb electromagnetic waves at a specific frequency. FTIR absorption data always graphs as a dependent variable for "wavenumber." Wavenumber is a reciprocal of wavelength (i.e., wavenumber = 1/wavelength) [111]. After 28 days of osteoblast mineralization experiments, the molecular structure of the mineralized scaffolds was examined using Fourier-transform infrared technique (Thermo Nicolet 6700 FTIR Spectrometer). FTIR transmittance spectra were acquired using an ATR. The spectra were recorded over the range 2000-500 cm^{-1}. The aperture was 150. The number of scans was 128 and resolution 0.4.

3.13 Raman Analysis of MAC-Lp scaffold for Osteoblast Formation

Raman Spectroscopy is a material characterization method that can characterize functional groups and chemical structures of a material. One advantage of this technique over FTIR is that there is no interference between water (OH peak) and other functional groups. This feature makes Raman very attractive for organic tissue characterization since they usually contain a high portion of water and molecules with many –OH groups [112]. The DXR Raman Microscope with laser at UTA's Characterization Center for Materials and Biology (CCMB) (DXR, Thermo

Scientific) was used to dehydrate samples of in-vitro cell cultures on the sample surface for 28 days with an ascorbic acid medium to induce cell differentiation to study the impact of the surface chemistry on mineral deposition with a 532-nm wavelength laser, 10 mW laser powder, 4-second exposure time, a 600- to 2000-cm^{-1} range limit and a 50 μm pinhole slit.

3.14 SEM-EDS of MAC-Lp scaffold for Osteoblast Formation

The Energy-dispersive X-ray spectroscope (EDS) is another detector that is usually available in SEM microscopes. When electrons from the SEM's electron gun hit the target atom and if the electron energy is sufficiently high, it can push out an electron from the inner shells and create an "electron hole." The electron hole is replaced by an electron from a higher shell which has higher energy. This difference in energy will generate a characteristic X-ray that is unique to that element. By collecting these X-ray beams, the element at the radiated point can be detected. Mapping element distribution on the surface is also possible by using scanning electron beams [110]. Mapping of the scaffold was observed with the Hitachi S-3000N Variable Pressure SEM (CCMB). The scaffold with cells was treated for 28 days to observe osteoblast formation. After dehydration, the desired samples were prepared with the sputtering systems: CrC-100 was available for coating conductive silver layers on the non-conductive samples for SEM observation and analysis by the Hitachi S-3000N Variable Pressure SEM (Characterization Center Materials and Biology) in 20 kV and 25 kV voltage environments. Both morphology and spectra using EDS were observed.

RESULTS AND DISCUSSION

4.1 Methacrylated Gelatin Synthesis

The FTIR results were confirmed to be a successful methacrylation reaction. There was an amide peak in MAG when comparing the gelatin shifting toward higher wavenumbers. This was a characteristic shift of MAG [112]. The amino group of the gelatin was converted to the amide group. The aim of methacrylation was to incorporate C=C into the structure. The methacrylate group of MA had C=C. Moreover, the methacrylate group of MA was added to the amino group of gelatin. Absorption peaks were observed at 1525 and 1061 cm-1. They were assigned to the N–H stretch of the Amide (II) group and to the C–O stretch, correspondingly. The spectrum of MAG showed absorption bands similar to those found in the gelatin spectrum (Figure 4.1) at 3295 and 2926 cm-1. These belonged to the N–H stretch of Amide (II) and the C–H stretch, respectively. The peaks at 1633 and 1228 cm-1 were directed to the C=O stretching vibrations of the MAG amide group and the N–H bending of Amide (III) [113].

a) b)

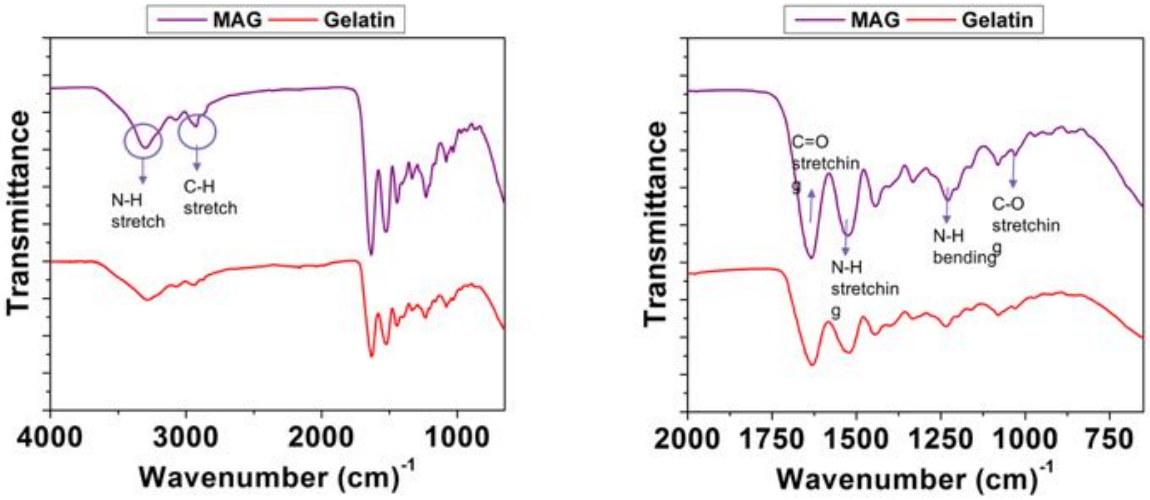

Figure 4.1 (a) FTIR results of gelatin and MAG range between 4000 and 500 cm^{-1}. (b) FTIR results with zoom version within range of 2000 to 500 cm^{-1}

4.2 Methacrylated Chitosan Synthesis

The same mechanism was valid for MAC and chitosan. The aim of the methacrylation process was to incorporate C=C bonds into the amino group of the chitosan. The main bands in this spectrum were stretching vibrations of the OH group. They overlapped since the OH stretching vibration covered 3750 to 3000 cm^{-1}. The C-H bond in $–CH_2$ was 2920 cm^{-1} and in CH_3, it was 2871 cm^{-1}. Methylene and the methyl groups were assigned 1374 cm^{-1} and 1418 cm^{-1}, respectively [113]. Vibrations of the C=O bonds were assigned 1651 cm^{-1} [114]. Asymmetric vibration of C-O was from 1150 to 1050 cm^{-1}. The small peak at 894 cm^{-1} corresponds to the saccharide structure [115].

Freeze dried MAC was performed to characterize the use of FTIR. Methacrylated chitosan bands were seen at 1651 cm^{-1}. They were assigned C=C bonds. 3272, 2921, and 1651 cm^{-1} belong to the O-H, C-H, and C=O stretched of MAC amide groups, respectively [79].

a) b)

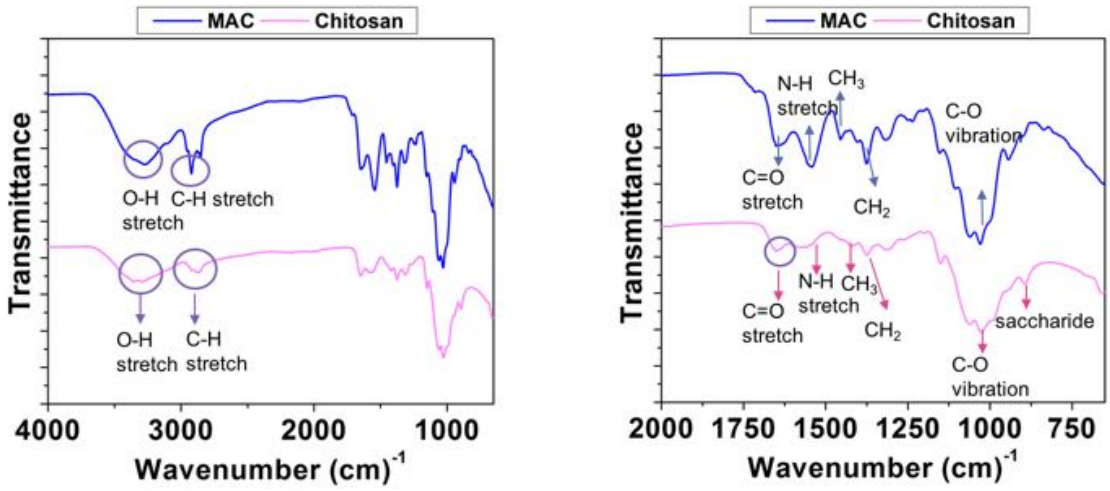

Figure 4.2 (a) FTIR results of gelatin and MAG range between 4000 and 500 cm^{-1}. (b) FTIR results with zoom version within a range of 2000 to 500 cm^{-1}

Figure 4.3 Gross shape of MAG and MAC products. Left ones are MAG, and the right ones are MAC.

4.3 Injectability Evaluation

Injectability was achieved with different mixing times and temperatures. Suitable parameters were found for three-dimensional printing below.

Composition	Temperature	Stirring Time	Mixing Time	Mixing Speed
MAG	**80 °c**	**3 mins**	**15 mins**	**2000 rpm**
MAG- Lp	**80 °c**	**3 mins**	**15 mins**	**2000 rpm**
MAC	**65 °c**	**3 mins**	**30 mins**	**2000 rpm**
MAC – Lp	**80 °c**	**3 mins**	**30 mins**	**2000 rpm**

Table 4.1 Schematic diagram of temperature, time, and speed for MAG, MAG-Lp, MAC, and MAC-Lp scaffolds

4.4 Rheological Properties and Dynamic Mechanical Properties

Comparisons of MAC, MAC-Lp, MAG, and MAG-Lp on the rheological properties inks were evaluated by oscillatory shear experiments at 25°C. Oscillatory stress sweep experiments were performed to investigate dynamic moduli. Increasing shear stress was applied to the sample, and the storage G′ and loss G″ were measured. As shown in Figure 4.4, the storage modulus G′ and the loss modulus G″ evolution of the inks with Laponite content is a function of tanδ, which is a measure of the internal friction of the material.

The tangent of the phase angle is the ratio of the loss modulus (G") to the storage modulus (G').

Tan delta values of less than unity indicate elastic-dominant (i.e. solid-like) behavior, and values greater than unity indicate viscous-dominant (i.e., liquid-like) behavior [116]. G′ and G″ increased monotonically by increasing the amount of laponite. Figure 4.4 shows a broad linear region known as the viscoelastic region with the storage modulus (G′) being always larger than the loss modulus (G″). It shows viscoelastic behavior. The influence of laponite concentration on the moduli of ink can be easily understood. Storage and loss moduli increase with an increase in laponite concentration. The reason for this may be viscosity synergism between hydrogel and laponite being electrostatic interactions between the negatively charged silanol (Si – O – H) groups on the silicate layers of laponite and the positively charged amide group of hydrogels [117].

There was an expectation to have highest shear and loss modulus of MAG-Lp to MAC-Lp, which may be due to the existing laponite and crosslinking mechanism [118].

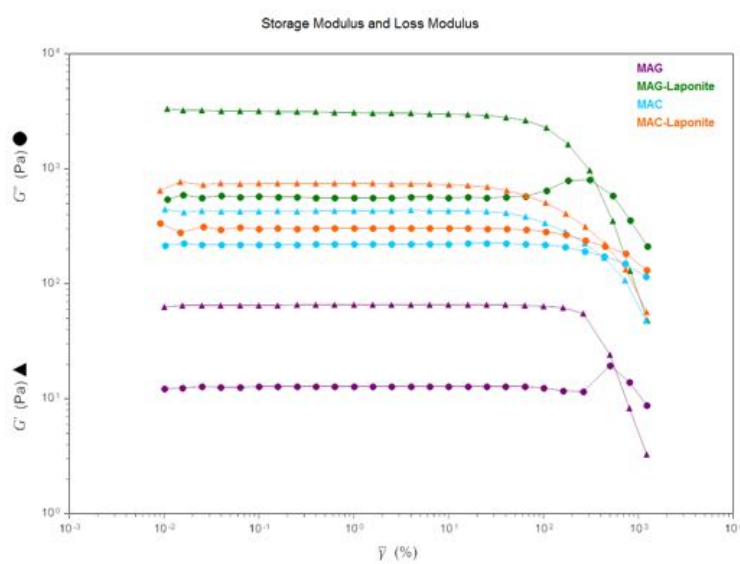

Figure 4.4 Storage Modulus (G′) and Loss Modulus (G″) of MAC, MAC-Lp, MAG, MAG-Lp inks

The same mechanism was valid for viscosity. After determining the injectability, the viscosity of the hydrogel was measured. Figure 4.5 shows that every ink illustrates shear thinning behavior under deformation. Existing silicate based ceramic which is laponite is significantly affected by the viscosity of hydrogels [119]. The viscosity of the MAG-Lp and MAC-Lp hydrogels increased monotonically upon increasing the laponite content. The polymerization was expected to occur on the surface of the laponite disk-like particles. The increase of viscosity was due to the enhancement of the cross-linking density [120].

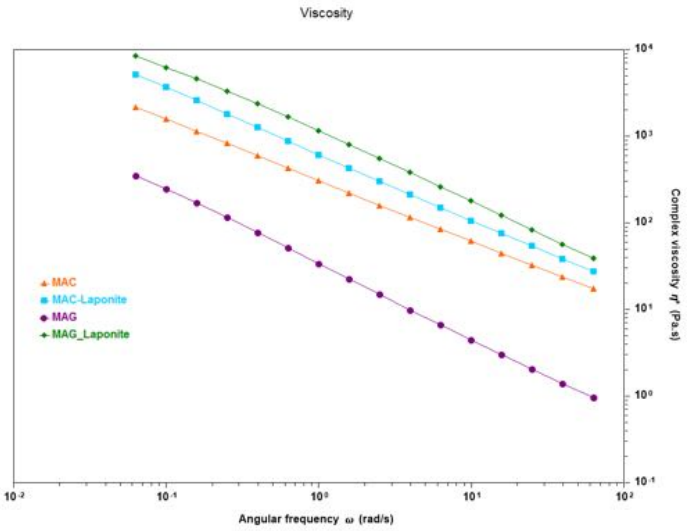

Figure 4.5 Viscosity properties for MAC, MAC-Lp, MAG, MAG-Lp inks

4.5 Adjusting Material and Printing Setting

The optimum setting and material composition was achieved by evaluations based on the Z-distance from the substrate and from the speed. Previous studies gave ideas about debubbling and the Z-distance for each layer. The summary of every attempt is listed in Tables 4.2 and 4.3. For each setting, a set of 10 attempts was performed. For each attempt, the shape of the scaffold remained the same, i.e., rectangular. If every attempt had failed, the result would be recorded as an unsuccessful printing. It was attempted to be done when every attempt succeeded.

Z distance from substrate from starting point for MAG and MAG-Lp	Printing achieved	Reason
Touching the surface	No	The material was not extruded. Pressure built up and a burst extrusion occurred in the second layer.
0.1 mm	No	The first layer was completely covered with filament. There was no porosity between the filaments.
0.2 mm	Yes	Results were taken as suitable for the design.
0.22 mm	No	The filaments were fluctuating.

Table 4.2 Attempts to evaluate the optimum distances between the substrate and dispenser tip for MAG and MAG-Lp

Z distance from substrate from starting point for MAC and MAC-Lp	Printing achieved	Reason
Touching the surface	No	The material was not extruded. Pressure built up and a burst extrusion occurred in the second layer.
0.1 mm	No	First layer was all covered with filament. There was no porosity between the filaments.
0.2 mm	No	Porosity was not qualified.
0.22 mm	Yes	The filaments were printed as a design.
0.3 mm	No	The filaments were distorted.

Table 4.3 Attempts to evaluate the optimum distances between the substrate and dispenser tip for MAC and MAC-Lp

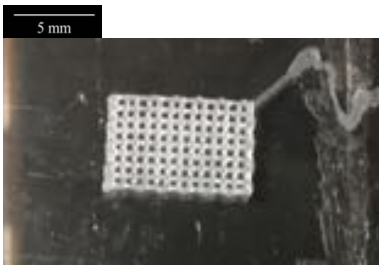

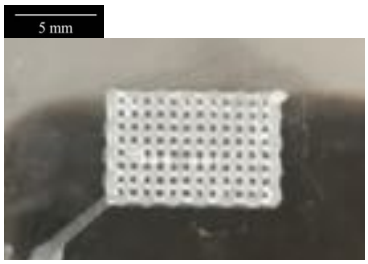

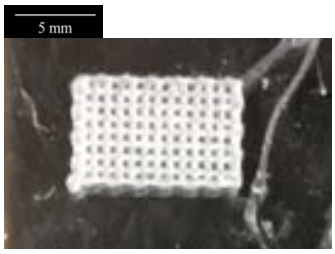

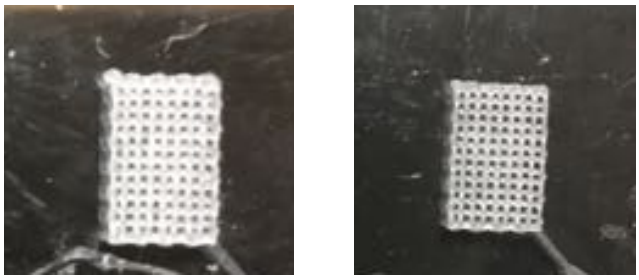

Figure 4.6 Gross shape of the bio-ink scaffold. The resolution of pores in the scaffold 450±50μm

4.6 Minimum UV Intensity for Ink Crosslinking

4.6 Minimum UV Intensity for Ink Crosslinking

Two group of scaffolds crosslinked by 30 and 40 mW/cm2 remained intact in the environment after 28 days. 30 mW/cm2 was selected to be applied to all 4 groups. This intensity value was chosen is previous study regarding UV intensity value for MAG-Lp. It was examined that MAG-Lp scaffolds below 30 mW/cm2 were dissolved. This value for MAG-Lp was guided to be determined MAC-Lp intensity value. In this thesis, it was aimed to get equal same mechanical behavior for groups with/without laponite. It is known that UV intensity is directly related with mechanical properties [122]. When it was applied to mechanical test to 30 mW/cm2 MAC-Lp and 40 mW/cm2 MAC-Lp samples, compressive strength of 30 mW/cm2 MAC-Lp was the same value with compressive strength of 30 mW/cm2 MAG-Lp. Finally, 30 mW/cm2 was determined as an intensity value to be applied to all four groups.

Intensity	**10 mW/cm^2**	**20 mW/cm^2**	**30 mW/cm^2**	**40 mW/cm^2**
MAG – Lp	Dissolved	Not Dissolved	Not dissolved	Not dissolved
MAC – Lp	Dissolved	Dissolved	Not dissolved	Not dissolved

Table 4.4 Schematic diagram of various UV intensities for MAG-Lp and MAC-Lp

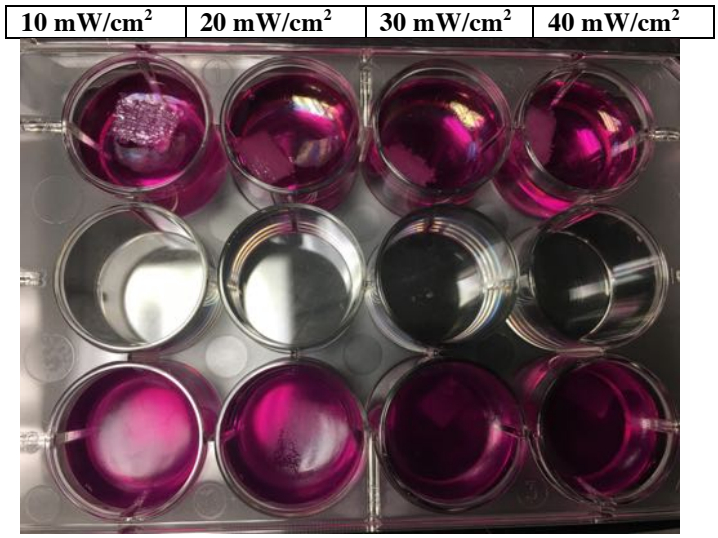

Figure 4.7 Effect of real-time UV illumination intensity on scaffolds immersed with α - MEM (Day 1). First group is MAC-Lp, second is MAG-Lp

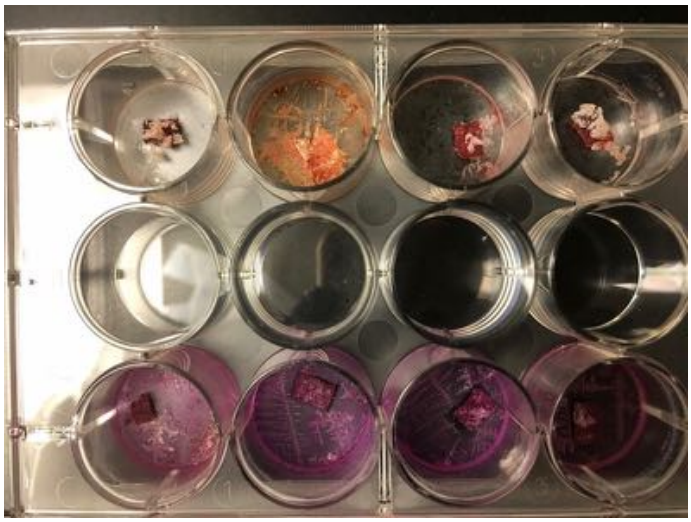

Figure 4.8 Effect of real-time UV illumination intensity on scaffolds immersed with α - MEM (Day 28). First group is MAC-Lp, second is MAG-Lp

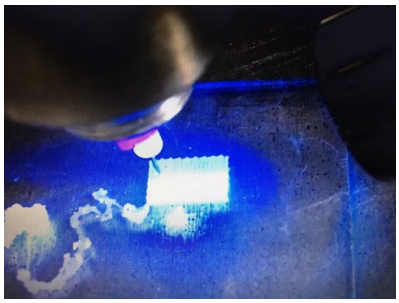

Figure 4.9 Photopolymerization with UV light during printing scaffolds

4.7 Swelling Test

The swelling defines the rate at which fluid infiltrates the scaffold. All scaffold exhibited an increase in weight when they were immersed in the DPBS solution. Without the laponite, the group showed the highest swelling rate of 20.20% ± 0.29 for MAG and 30.17% ± 1.36 for MAC, which was significantly higher than all other samples.

Results may be explained with the hydrophilic group in the chitosan and gelatin backbone and crosslinking mechanism. The backbones are easily hydrated. In addition, MAC has less of a crosslinking mechanism, but its water diffusion was faster than the MAG scaffolds [121]. It was also reported that the content of the laponite caused the decrease in the swelling ratio [122].

MAG	Dry Weight (gr)	Wet Weight (gr)	% Swelling
Sample 1	0.0157	0.0189	20.38
Sample 2	0.0162	0.0195	20.37
Sample 3	0.0156	0.0187	19.87

Table 4.5 % swelling of MAG with different compositions after immersion in DPBS

MAG – Lp	Dry Weight (gr)	Wet Weight (gr)	% Swelling
Sample 1	0.0159	0.0179	12.57
Sample 2	0.0153	0.0173	13.07
Sample 3	0.0153	0.0173	13.07

Table 4.6 % swelling of MAG-Lp with different compositions after immersion in DPBS

MAC	Dry Weight (gr)	Wet Weight (gr)	% Swelling
Sample 1	0.0125	0.0167	33.6
Sample 2	0.0215	0.0287	33.48
Sample 3	0.0239	0.0315	31.17

Table 4.7 % swelling of MAC with different compositions after immersion in DPBS

MAC – Lp	Dry Weight (gr)	Wet Weight (gr)	% Swelling
Sample 1	0.0341	0.0381	11.7
Sample 2	0.0397	0.0442	11.33
Sample 3	0.0247	0.0278	12.55

Table 4.8 % swelling of MAC-Lp with different compositions after immersion in DPBS

4.8 Mechanical Properties

The mechanical properties of the matrix environment were shown to affect cell function and differentiation [123]. To determine the fixation compressive strength among the scaffolds of all the groups with and without laponite, 30 mW/cm^2 and 40 mW/cm^2 UV light was applied to the MAC-Lp group. It was shown that MAC-Lp, which had 30 mW/cm^2 UV light applied to it, was of the same compressive strength as the MAG-Lp group, which had 30 mW/cm^2 UV light applied to it.

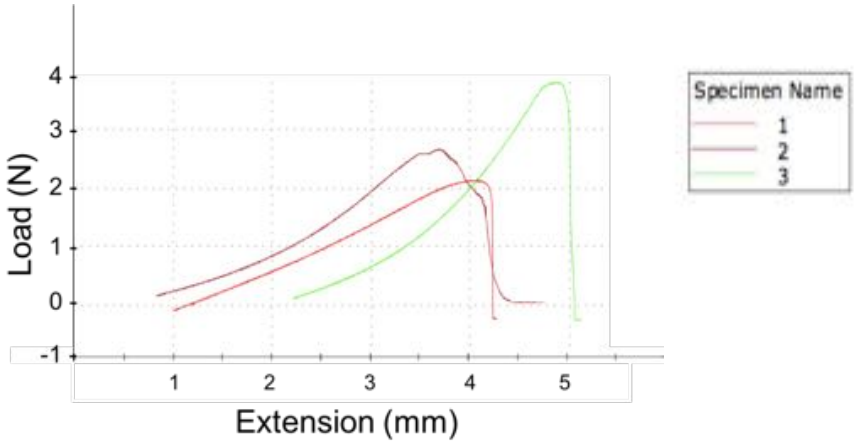

Figure 4.10 Mechanical properties of MAG-Lp 30 mW/cm^2, MAC-Lp 30 mW/cm^2, and MAC-Lp 40 mW/cm^2. Specimen name 1 is MAG-Lp 30 mW/cm^2, name 2 is MAC-Lp 30 mW/cm2, and Specimen name 3 is MAC-Lp 40 mW/cm^2.

Later, 30 mW/cm^2 was determined to be applied to the MAC-Lp and MAC group scaffolds.

Groups	MAG	MAG-Lp	MAC	MAC-Lp
n=1 (Mpa)	6	11.8	8.85	13.79
n=2 (Mpa)	8.85	16.9	6.88	15.45
n=3 (Mpa)	7.1	13.66	6.92	12.98
average	7.317	14.12	7.55	14.073
std dev	2.015	2.580	1.126	1.2591

Table 4.9 Compressive strength values (n=3) for MAG, MAG-Lp, MAC, and MAC-Lp scaffolds with averages, and standard deviations

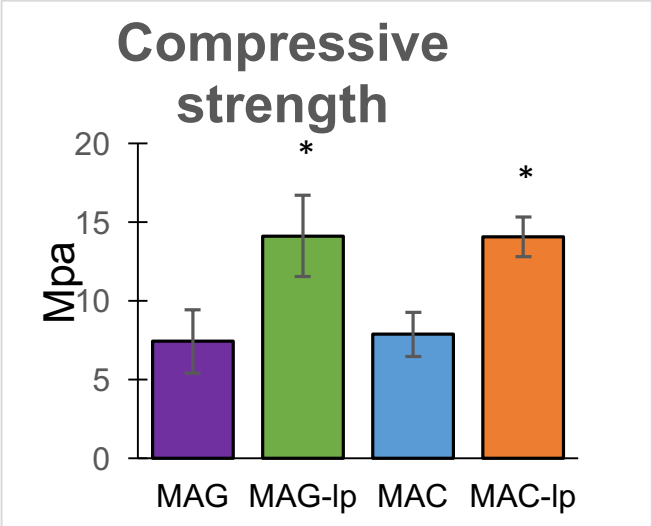

Figure 4.11 Graphical demonstration of mechanical properties of all scaffold groups

Compressive Strength (Mpa)	MAG	MAG-Lp	MAC	MAC-Lp
average	7.317	14.12	7.55	14.073
std dev	2.015	2.580	1.126	1.2591

Table 4.10 Averages and standard deviations of the mechanical properties of MAG, MAG-Lp, MAC and MAC-Lp discs

This stage was significantly crucial for this thesis. It can easily be said that a compressive strength of 10% wt MAC was equal to 20% wt MAG when applying the same UV light. Based on a previous study [118], it was shown that laponite enhanced the mechanical properties. This mode could be related to the relaxation of the laponite and polymer aggregates with the network. Again, the overall results suggest that the existence of laponite significantly influences the stress/relaxation behavior of the nanocomposite networks. Recovery and stress relaxation of a physical network between laponite and polymer is important in determining the self-healing properties of these materials [124].

In its natural hydrated state, cortical bone has a compressive strength (σ) of 110-150 MPa, while cancellous bone has a compressive strength 2-6 MPa [125]. Based on these results, it is easily seen that these four groups can be utilized to replace cancellous bone replacements.

4.9 Scaffold Surface Analysis

The samples were printed with three dimensional printers and then dried for one hour. After selection, various magnifications were performed by a stereo zoom microscope scaffold. Images were taken using the Large Fields Fluorescence Stereo Zoom Microscope (Axio Zoom.V16, ZEISS, US). The images were captured at 7×, 25×, 63×, 80× and 125× magnifications.

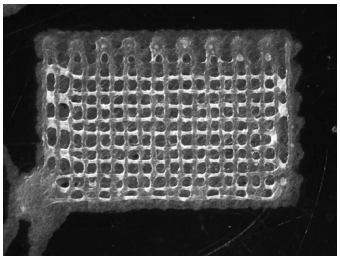
7X

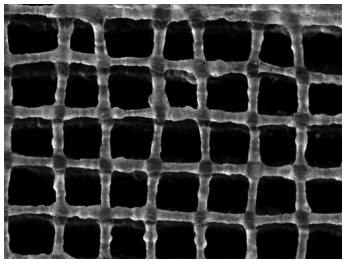
25X

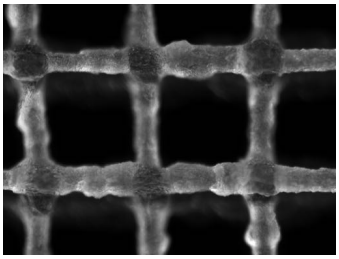
63X

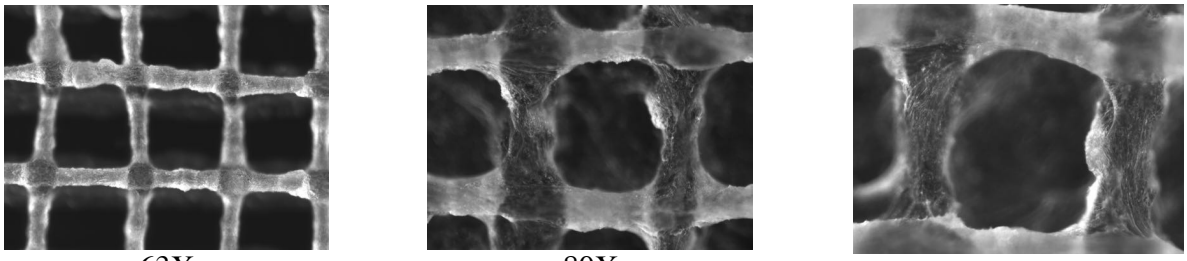

63X 80X 125X

Figure 4.12 Various magnifications with the Stereo Zoom Microscope images of MAC and MAC-Lp scaffolds.

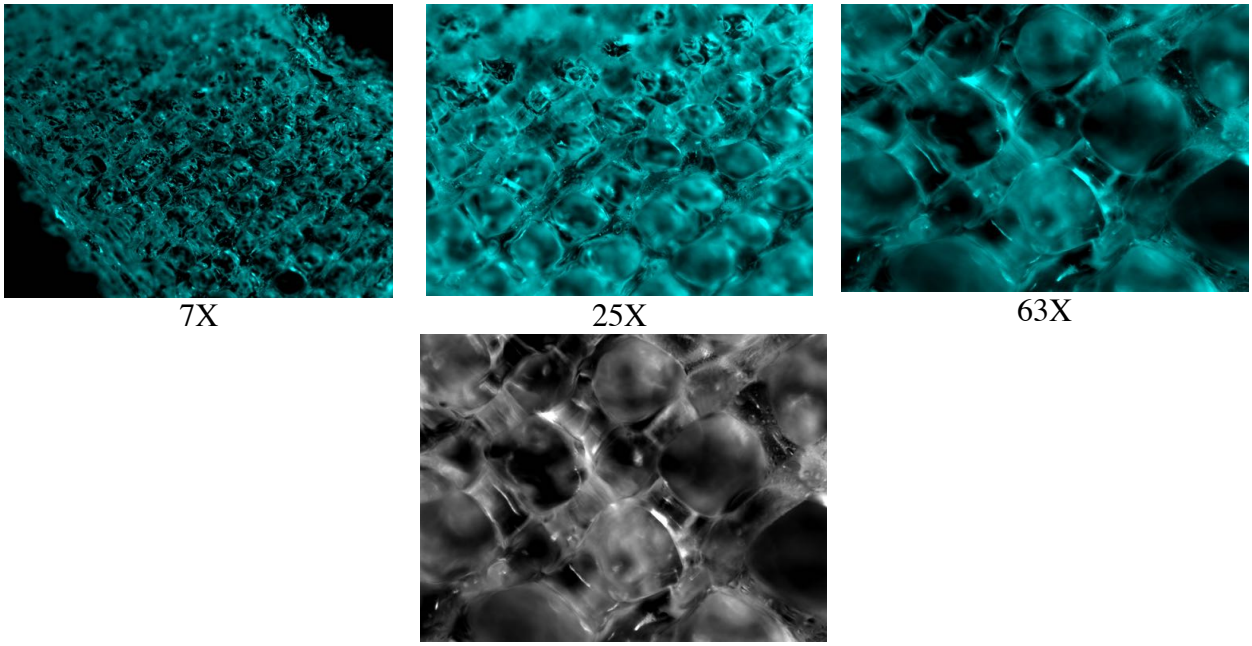

7X 25X 63X

63X

Figure 4.13 Various magnifications with Stereo Zoom Microscope images of MAG and MAG-Lp scaffolds.

The samples were printed with three dimensional printers and then dried for one day. After selection, they were sputtered with silver on the top of the bioactive porous scaffold. An image was taken by the Hitachi S-3000N Variable SEM. The pore size of scaffold was designated 450 μm. The filament was designated as 250 μm. Average filament size was 118.5 ±12.19 μm. The pore sizes were 389 ± 58 μm based on horizontal, 385 ± 38 μm based on vertical. The reason that might be shrinkage of scaffold after printing. It was difficult to storage the scaffolds after

printing. %100 ethanol was used to keep scaffolds.

Average filament size was 267.5 ±23 µm of MAG-Lp scaffold. The pore sizes were 530 ± 21 µm based on horizontal, 450 ± 25 µm based on vertical.

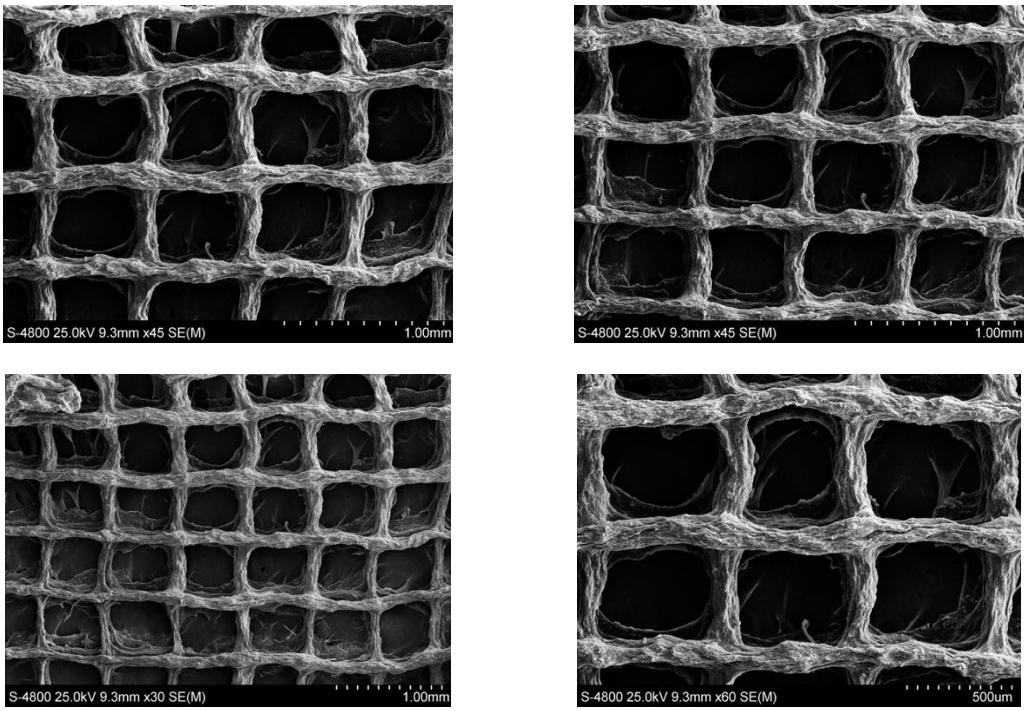

Figure 4.14 Scanning Electron Microscope (SEM) images of MAC-Lp scaffolds, 25 kV voltage, ×30, ×45 and ×60 magnifications

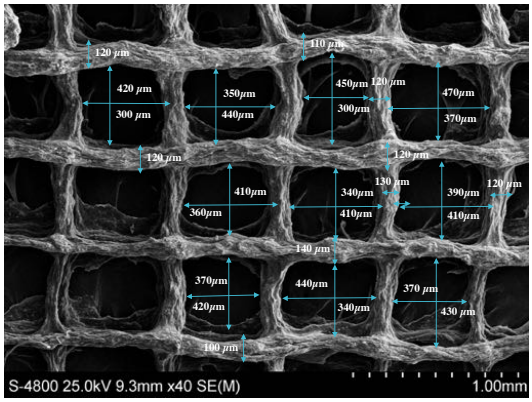

Figure 4.15 Porous size of MAC-Lp scaffold. Average filament size was 118.5±12.19 µm. The

pore sizes were 389 ± 58 μm based on horizontal, 385±38 μm based on vertical.

Porosity of MAC-Lp (μm)	Horizontal	Vertical
Average	389	385
Standard Deviation	58	38

Table 4.11 Averages and standard deviations of MAC-Lp scaffold based on horizontal and vertical

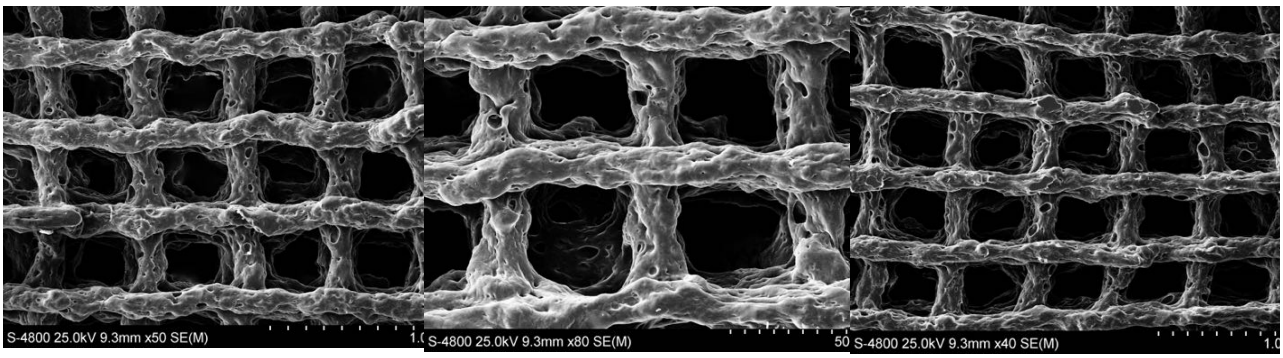

Figure 4.16 Scanning Electron Microscope (SEM) images of MAG-Lp scaffolds, 25 kV voltage, ×40, ×50 and ×80 magnifications

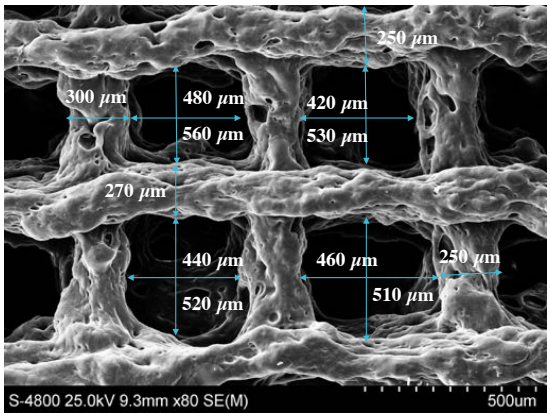

Figure 4.17 Porous size of MAG-Lp scaffold. Average filament size was 267.5 ± 23 μm. The pore sizes were 530 ± 21 μm based on horizontal, 450 ± 25 μm based on vertical

Porosity of MAG-Lp (μm)	Horizontal	Vertical
Average	530	450
Standard Deviation	21	25

Table 4.12 Averages and standard deviations of MAG-Lp scaffold based on horizontal and vertical

4.9 Control Media and Cell Culture

4.9.1 Cell Attachment

The attachment of the MC3T3-E1 subclone 4 cells to the MAC-Lp and MAG-Lp scaffolds are shown in Figures 4.15 and 4.16. A Representative Stereo Zoom Microscope view of the cells on the test and control specimen are shown in Figure 4.15. Cells on the control tissue culture plate exhibited a rounded unspread morphology. The MC3T3-E1 subclone 4 cells extended and spread on the chitosan based and gelatin based scaffolds.

a) b) c)

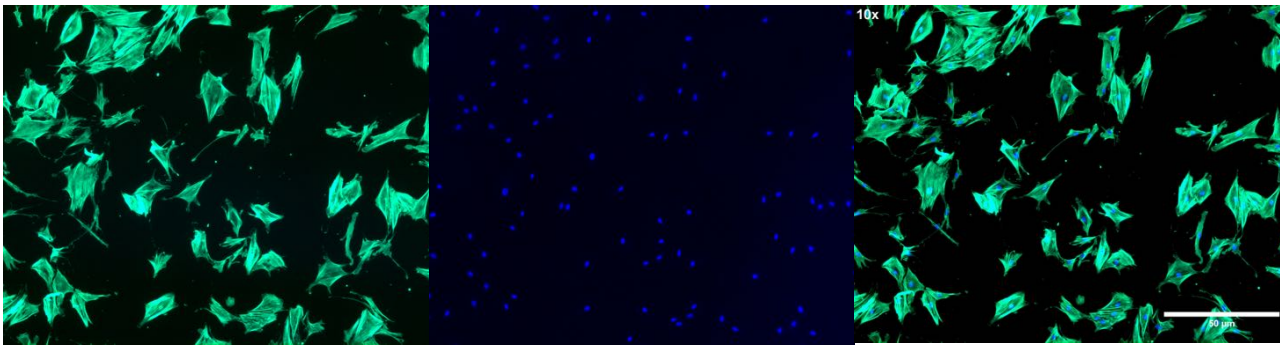

Figure 4.18 Cell attachment to tissue culture plate a) 10× magnification Phalloidin 488 (actin), b) 10× magnification DAPI, c) 10× magnification combined with Phalloidin 488 (actin) and DAPI

a) b) c) d)

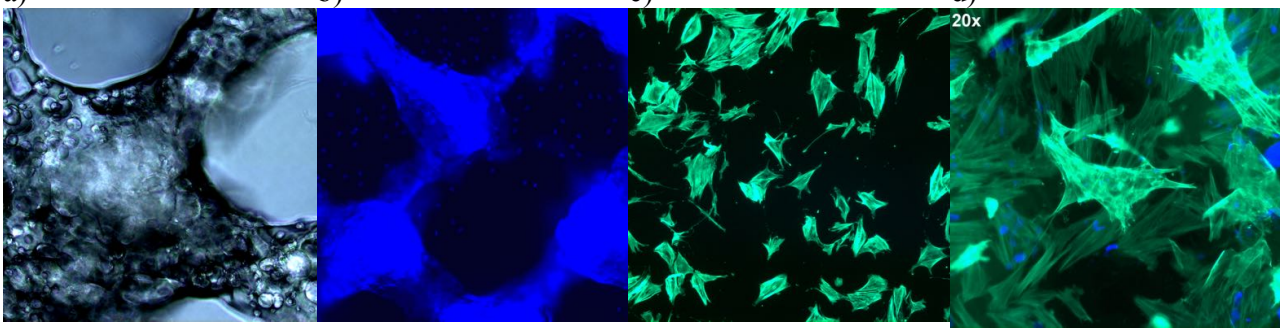

e) f) g) h)

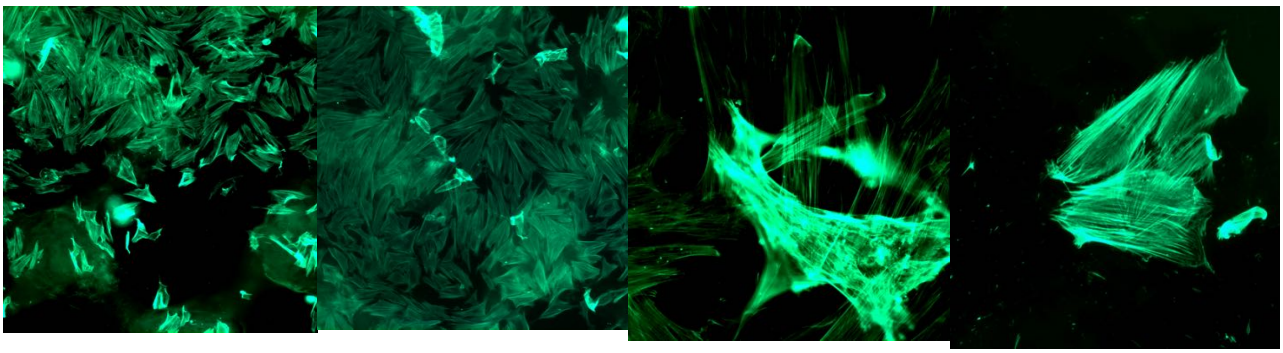

Figure 4.19 Various magnifications of cell attachment MAC-Lp scaffolds. a) 5× bright field, b) 5× DAPI, c) 5X- Phalloidin 488 (actin), d) 20× Combined with DAPI and Phalloidin 488 (actin), e) 10× Phalloidin 488 (actin), f) 10× Phalloidin 488 (actin), g) 40× Phalloidin 488 (actin), h) 40× Phalloidin 488 (actin)

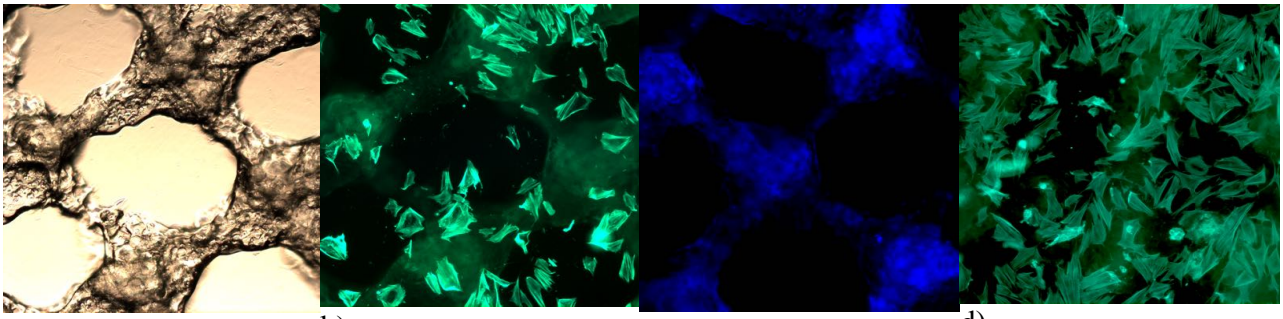

a) b) c) d)

e) f) g) h)

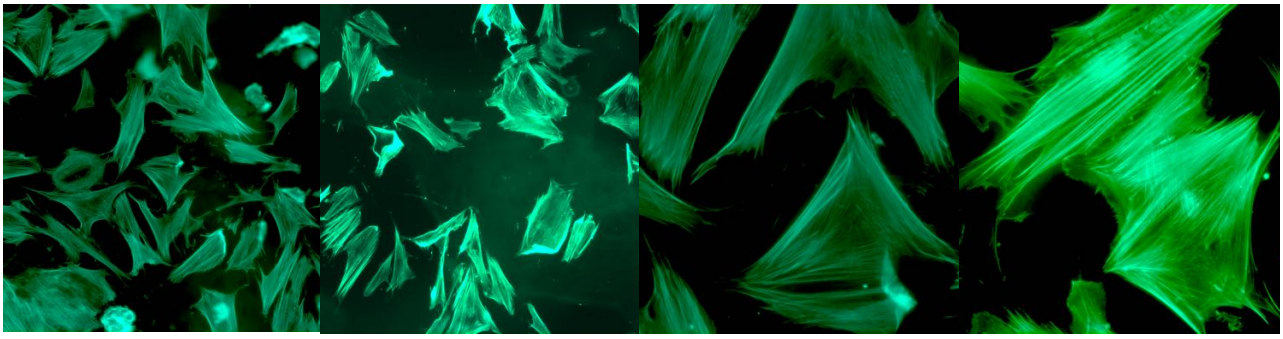

Figure 4.20 Various magnifications of cell attachment MAC-Lp scaffolds. a) 5× bright field, b) 5× DAPI, c) 5×- Phalloidin 488 (actin), d) 20× Combined with DAPI and Phalloidin 488 (actin),

e) 10× Phalloidin 488 (actin), f) 10× Phalloidin 488 (actin), g) 40× Phalloidin 488 (actin), h) 40× Phalloidin 488 (actin)

4.9.2 Cell Viability

Measurements for cell viability were used to evaluate the viable cells. Cell viability assays were also often useful in determining optimal growth conditions of cell populations maintained in a culture. An MTS reagent was used in the cell viability measurement. The assay is based on the reduction of an MTS tetrazolium compound by viable cells to generate a colored formazan product (purple) that is soluble in cell culture media. This conversion is thought to be carried out by NAD(P)H-dependent dehydrogenase enzymes in metabolically active cells. The formazan dye produced by viable cells can be quantified by measuring the absorbance by 490 nm, SpectraMax Plus, Molecular Devices (San Jose, Calif.). All groups were treated with regular media (a- minimum essential medium, a- MEM; 0.1% fetal bovine serum, FBS; and 1% penicillin-streptomycin, pen-strep). Based on the measurements, the MAC and MAC-Lp groups showed more than 2 times improvement of cell viability compared to the other groups ($p<0.001$) Basically, osteoingration and bone formation consist of 3 stages: Recruitment and attachment of osteoblast from bone tissue, proliferation and differentiation of osteoblast, and finally mineralization of a collagenous matrix [126]. Overall, the viability shows that all scaffolds can prove a great substrate for cell to attach and stay alive. This experiment can mimic the first stage of osteoingration.

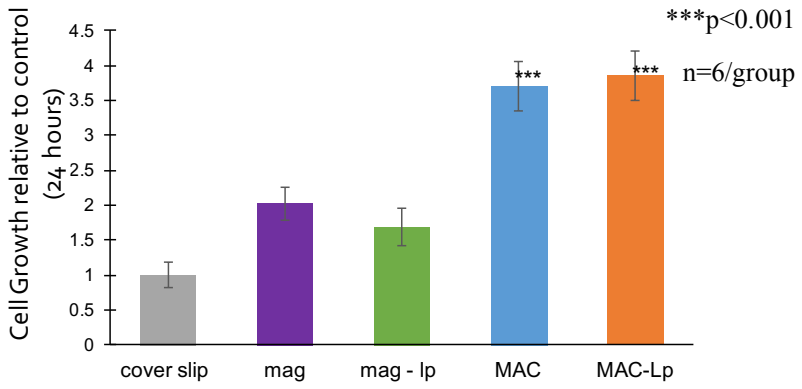

Figure 4.21 Cell viability of the MC3T3-E1 subclone 4 cell with tissue culture plate and scaffold groups which are MAG, MAG-Lp, MAC, MAC-Lp, viability 1 day ***p<0.001 n=6/group

4.9.3 Cell Proliferation

Cell Proliferation Assay measures the cell proliferation rate and the metabolic activity of cells. The method is similar to cell viability assay on the concept of cell study. The only difference is that the serum was treated in the medium. The serum can help cells to grow more and in a differentiated manner. The medium (α-minimum essential medium, α- MEM; 10% fetal bovine serum, FBS; and 1% penicillin-streptomycin, pen-strep) was used for testing cell viability for 1, 3, and 7 days. Every printed scaffold presented a significant enhancement to cell proliferation ($p<0.05$) on proliferation after 1 day. The MAC-group demonstrated a significant increase in cell numbers compared to the other groups ($p<0.01$) on proliferation after 1 day. The MAC-Lp showed an increase in cell growth compared to the cover slip, MAG and MAG-Lp ($p<0.05$) on proliferation after 3 days. After 7 days, the MAG-Lp, MAC and MAC-Lp groups showed a significant enhancement in cell growth relative to the control (cover slip) and MAG groups

(p<0.05); the MAC-Lp group presented a significant improvement in cell growth compared to the other groups (p<0.01)

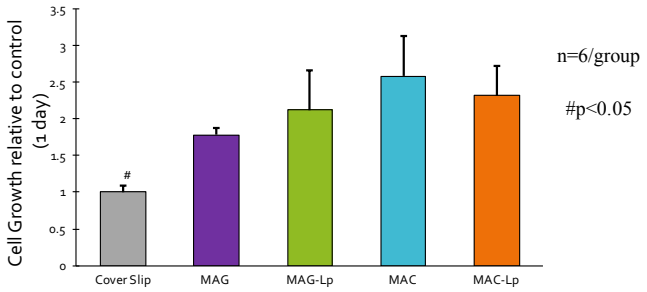

Figure 4.22 Relative cell growth of the MC3T3-E1 subclone 4 cell with tissue culture plate and scaffold groups, proliferation 1 day #p<0.05 n=6/group

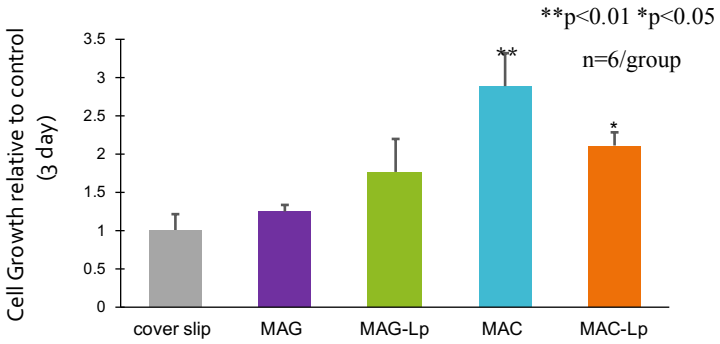

Figure 4.23 Relative cell growth of the MC3T3-E1 subclone 4 cell with tissue culture plate and scaffold groups, proliferation 3 days, **p<0.01 *p<0.05 n=6/group

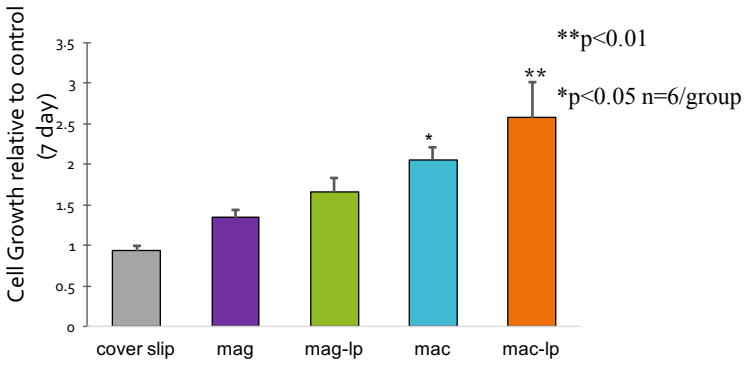

Figure 4.24 Relative cell growth of the MC3T3-E1 subclone 4 cell with tissue culture plate and scaffold groups, proliferation 7 days, **p<0.01 *p<0.05 n=6/group

The obtained results showed that the difference between gelatin and chitosan might be reflected in their degradation behavior. Previous studies have demonstrated that the material which included chitosan dissolved faster than the material without chitosan content [127]. Moreover, the differences between the MAG, MAG-Lp and MAC, MAC-Lp scaffolds lay in their crosslinking densities. Since MAC and MAC-Lp have less crosslinking density, they might degrade faster than the MAG, MAG-Lp scaffolds. The difference between MAC and MAC-Lp might be due to the release kinetic of laponite.

4.9.4 Collagen Analysis by SEM

The extra cellular matrix (ECM) is composed of an interlocking mesh of fibrous proteins and glycosaminoglycan. It includes proteoglycans (such as heparan sulfate, Chondroitin sulfate and keratan sulfate), non-proteoglycan polysaccharide such as hyaluronic acid and the most important fibers such as collagen fiber or some elastin fiber. SEM images illustrated the accumulation of the extra cellular matrix in Figure 4.26. After the cells grew, they secreted

ECM. The ECM was mineralized at least 21 days. When compared to a previous study, it obtained very similar results.

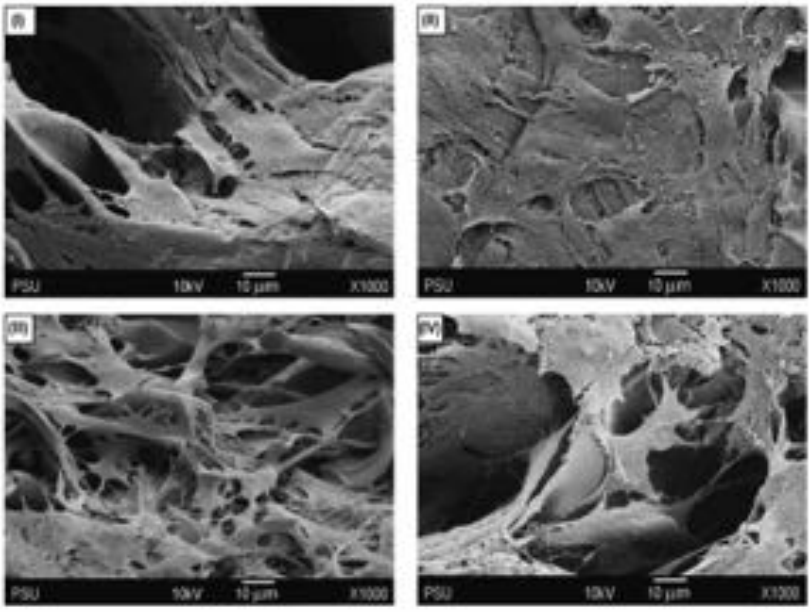

Figure 4.25 ECM collagen [1]

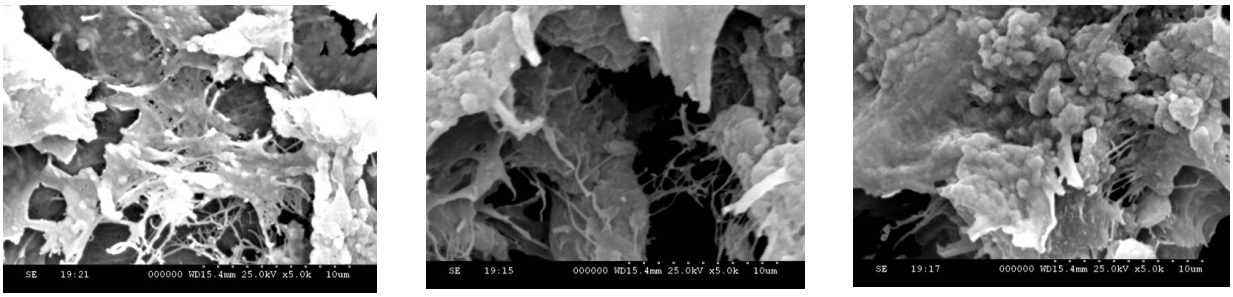

Figure 4.26 Collagen fiber in MAC-Lp scaffold

4.10 Fourier Transform Infrared Spectroscopy for Osteoblast Formation

The FTIR spectra of chitosan and gelatin based scaffolds can be seen in Figure 4.27. Differences are observed between those with and without Lp. (C = O) stretching (Amide I band) [128], at 1644 cm−1 for MAC-Lp and 1637 cm−1 for MAC, (N-H) bending in the primary amine and secondary amide (Amide II band) groups [129], at 1547 cm−1 for MAC-Lp and MAC,(C-O-C) stretching at 1050 cm−1 for MAC-Lp, 1055 cm−1 for MAC, and (C-N) and (N-H) stretching in

the tertiary amide (Amide III) groups at 1310 cm−1 for MAC-Lp, and 1239 cm−1 for MAC. These can be attributed to P-O symmetrical and asymmetrical stretching of phosphates, while the band at 989 cm−1 for MAC-Lp and 996 for MAC cm−1 arises from the P-O asymmetrical bending of PO4-3 molecules. [130].

a) b)

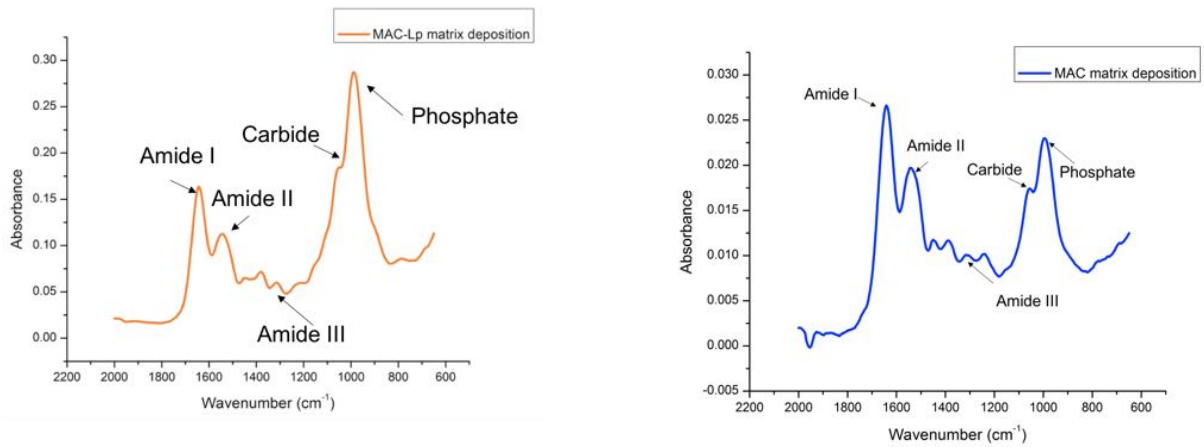

Figure 4.27 FTIR results for MAC-Lp and MAC scaffolds after 28 days matrix deposition. a) MAC-Lp scaffolds, and b) MAC scaffolds

a) b)

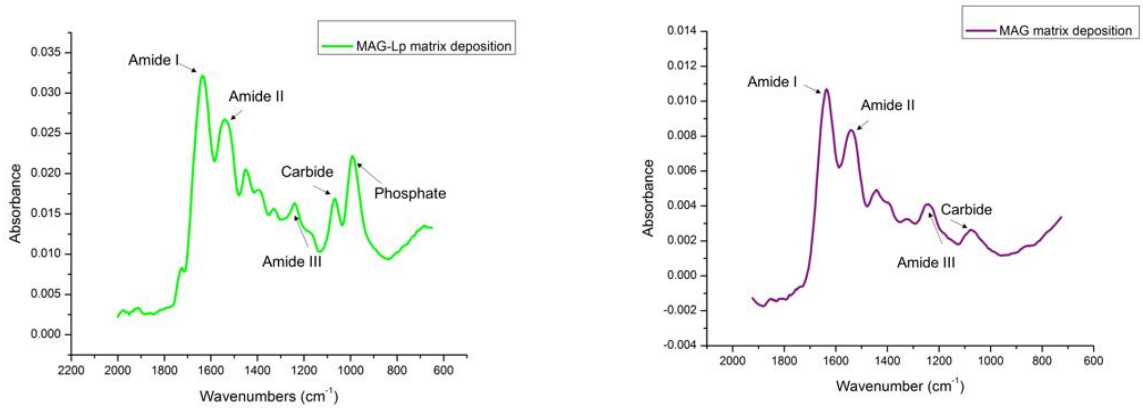

Figure 4.28 FTIR results for MAG-Lp and MAG scaffolds after 28 days matrix deposition.

a) MAG-Lp scaffolds and b) MAG scaffolds

The FTIR spectrum of the nanocomposite exhibited a number of characteristic spectral bands. Among them were protein spectra such as: N–H bending vibration at 1240 cm^{-1} for the Amide III for MAG-Lp, and 1247 cm^{-1} for MAG, N–H bending vibration at 1536 cm^{-1} is Amide II for MAG-Lp, and 1535 cm^{-1} for MAG, C=O stretching vibration at 1633 cm^{-1} is the Amide I for MAG-Lp, and 1637 cm^{-1} for MAG [131], (C-O-C) stretching at 1066 cm^{-1} for MAG-Lp. There was no significant (C-O-C) stretching peak for MAG. These can be attributed to P-O symmetrical and asymmetrical stretching of phosphates, while the band at 996 cm^{-1} for MAG-Lp arises from the P-O asymmetrical bending of PO_4^{-3} molecules. There was no significant P-O symmetrical and asymmetrical stretching peak for MAG [130].

To examine which group showed the highest osteoblast formation among all four groups, phosphate and Amide I ratios were taken. Based on the results, the highest ratio belonged to MAC-Lp, followed by MAC and MAG-Lp. There was no significant phosphate peak for MAG.

Highest peak	MAC-Lp	MAC	MAG-Lp	MAG
Phosphate	0.267	0.0192	0.022	No significant peak
Amide I	0.178	0.0288	0.033	0.0098
Phosphate/Amide I	1.5	0.67	0.67	N/A

Table 4.13 Phosphate and Amide I ratio of FTIR results for MAC-Lp, MAC, MAG-Lp and MAG

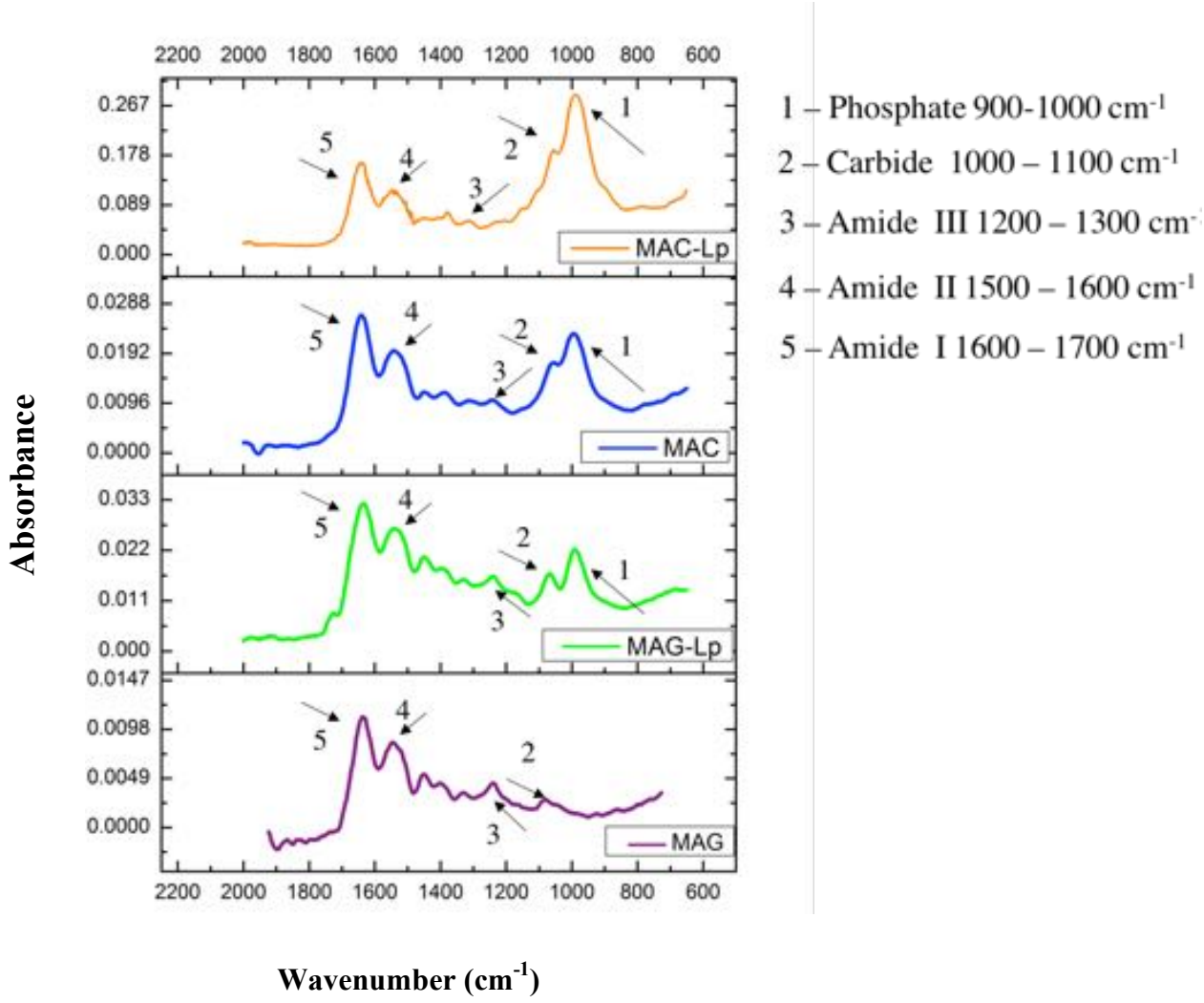

Figure 4.29 FTIR results for MAC-Lp, MAC, MAG-Lp and MAG scaffolds after 28 days matrix deposition

4.11 Raman Spectroscopy of MAC-Lp Scaffolds for Osteoblast Formation

Raman Spectroscopy is a material characterization method that can characterize the functional group and chemical structure of a material. The advantage of this technique over FTIR is that there is no interference between water (OH peak) and other functional groups. This feature makes Raman very attractive for organic tissue characterization since it usually contains a high portion of water and molecules with many –OH groups. In this spectrum, there is a band at

around 935 cm^{-1} which is related to phosphate. There are also Amide I and Amide III bands that represent organic components of bone and are located at 1662 cm^{-1} and 12456 cm^{-1}, respectively. The intensity ratio of Amide I or Amide III to the primary phosphate band represents the organic to mineral ratio (degree of mineralization) in the bone.

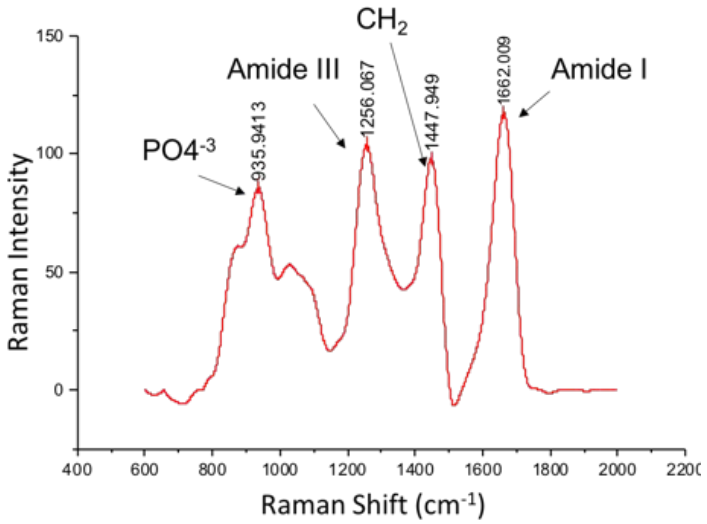

Figure 4.30 Raman result for MAC-Lp scaffolds. It was shown that there was phosphate, Amide I and Amide III bands.

Chitosan is a copolymer of glucosamine and N-acetyl-glucosamine. The N-acetyl-glucosamine in chitosan has a structural feature also found in glycosaminoglycans (GAGs). GAGs show many specific interactions with growth factors, receptors and adhesion proteins. The cationic nature of chitosan itself means that it can electrostatically interact with anionic proteoglycans, GAGs, and other negatively charged molecules [35]. In fact, chitosan has been reported to increase the ALP activity of osteoblasts and induce a significant increase in BMP-2 mRNA [135]. This significant increase is caused by the acceleration of osteoblastic cell proliferation [136]. Chitosan has also been reported to support the expression of extracellular matrix proteins in osteoblasts and the preferential attachment of osteoblasts over other cell types [137].

4.12 SEM – EDS of MAC-Lp Scaffolds for Osteoblast Formation

Surface morphology, scaffold composition and element distribution were investigated using a scanning electron microscope (Hitachi S-3000N Variable Pressure SEM) equipped with an energy dispersive X-ray spectrometry system (EDS). SEM images were taken at an acceleration voltage of 20.0 kV. EDAX software was used to quantify the spectral mapping data from vision areas. Regions of interest (ROIs) corresponding to Si, Mg, Na, Ca, and P K edges were defined for MAC-Lp scaffolds. We can identify that the Ca and P were obvious after the 28-day matrix deposition experiment.

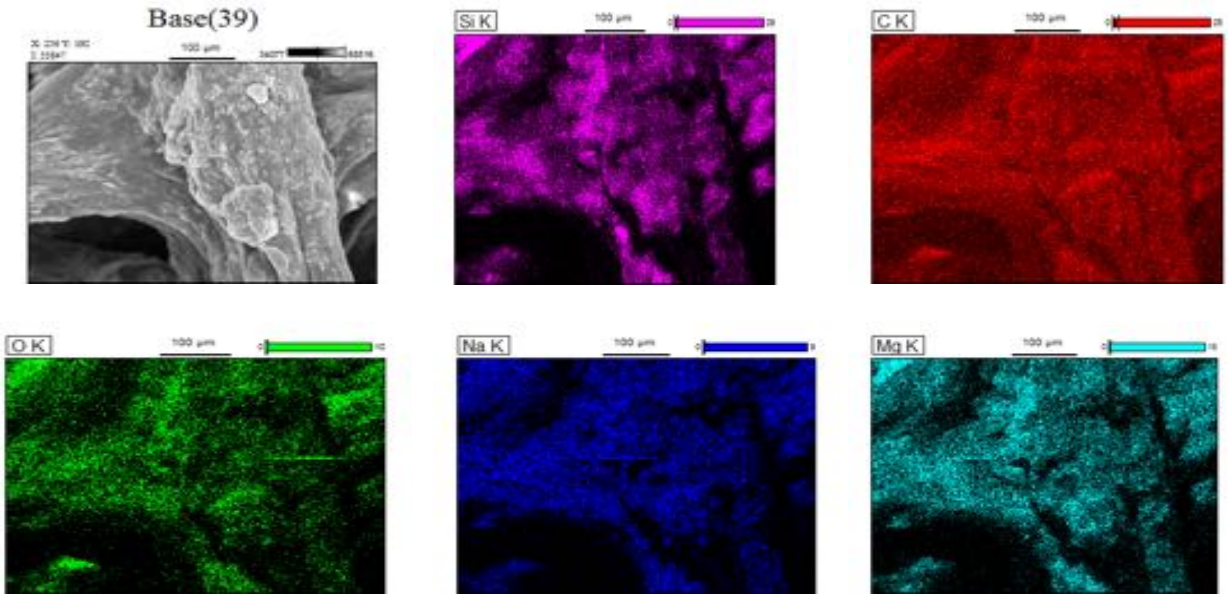

Figure 4.31 SEM-EDS of MAC-Lp scaffold before matrix deposition 20kV X250 magnification

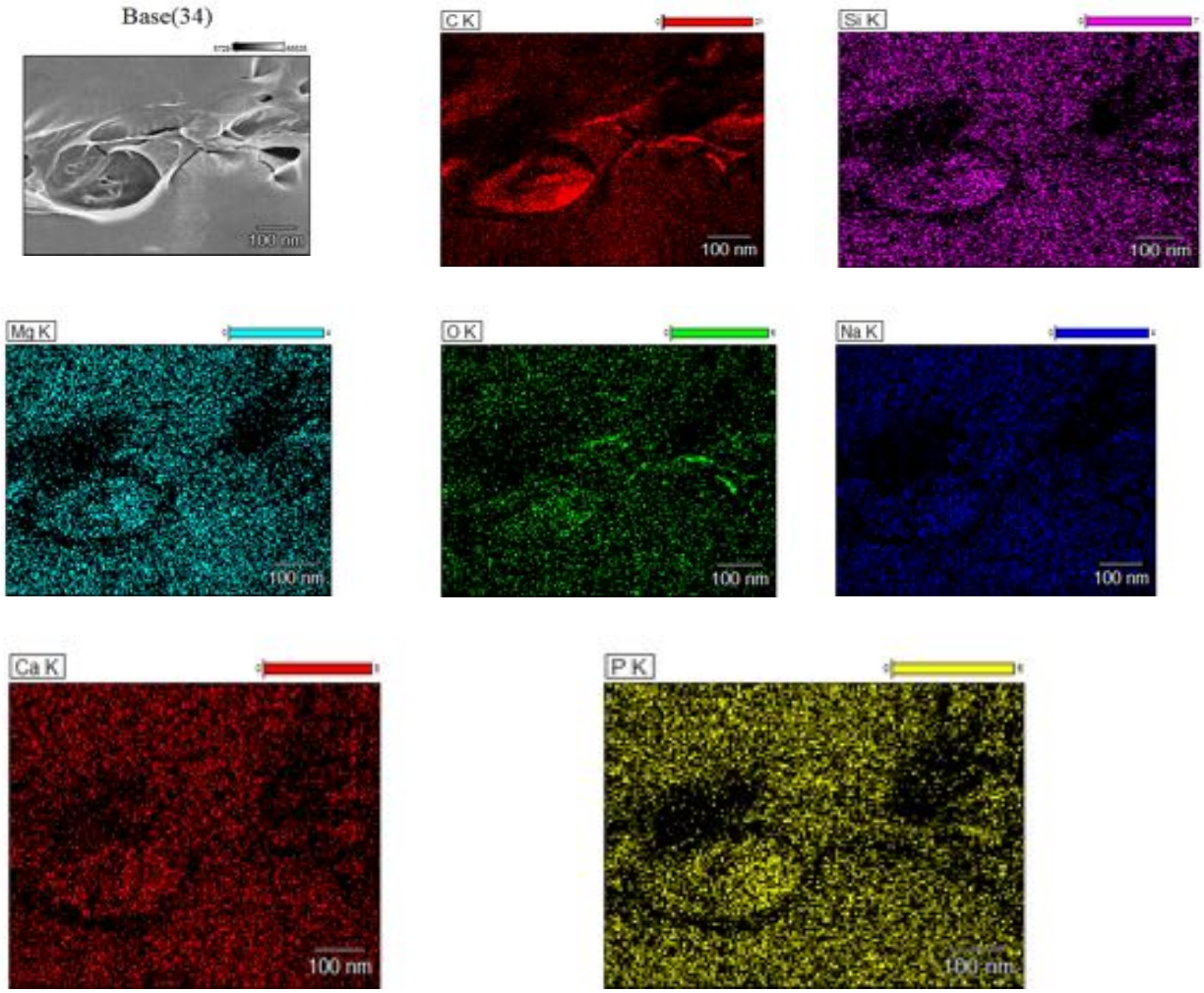

Figure 4.32 SEM-EDS of MAC-Lp scaffold before matrix deposition 30kV X180k magnification

CHAPTER 3

CONCLUSION

A biodegradable methacrylated chitosan (MAC) hydrogel was successfully synthesized. Methacrylate groups were incorporated into the amino groups of chitosan and fabricated as MAC scaffolds in 3D printing via UV photocrosslinking. Under 365-nanometer UV radiation and in the presence of the photoinitiator (Irgacure 2959), the methacrylate groups of chitosan were able to react with the hydroxyl group of photoiniators to form a crosslinked hydrogel.

Then it was integrated with 4 wt % laponite and 10 wt % MAC to create methacrylated chitosan-laponite (MAC-Lp). To make a comparison, synthesized methacrylated gelatin (20 wt % MAG) was integrated with 4 wt % laponite and to create methacrylated gelatin-laponite (MAG-Lp) and printed 3D scaffolds with UV photocrosslinking. The MAG-Lp scaffolds presented an average compressive strength of 7.31 MPa, which is comparable to human cancellous bone, which ranges from 2 to 6 MPa. This find demonstrates that MAC-Lp can be utilized to replace cancellous bone.

Rheological and mechanical properties indicated that the existing laponite increased the stiffness in both types of scaffolds (MAG-Lp and MAC-Lp).

Moreover, MAC-Lp showed no cytotoxicity to MC3T3-E1 subclone precursor osteoblast cells. In addition, MAC, and MAC-Lp scaffolds demonstrated two times the enhancement to cover slip, MAG, and MAG-Lp scaffolds. The newly developed MAC-Lp scaffold offers the advantage in terms of water solubility, as well as in terms of mechanical, rheological, and morphological properties.

Matrix deposition experiments were also applied to MAC, MAC-Lp and MAG, MAG-LP scaffolds and analyzed with the FTIR technique. Results showed that all scaffolds were able to

enhance the Amide I band. Except for the MAG scaffold, the remainder was able to enhance the Phosphate band. Based on their FTIR results, the Phosphate/Amide I ratios demonstrated that the highest ratio belonged to MAC-Lp.

Later on, the Raman, SEM and SEM-EDS technique were applied to the MAC-Lp scaffolds to show the Phosphate, Amide I, Amide III, and carbide bond in Raman, collagen fiber in SEM, and Ca, and the P atoms in SEM-EDS techniques. This may be due to the chitosan having been reported to increase the ALP activity of osteoblasts and to induce a significant increase in BMP-2 mRNA [135]. This increase was caused by the acceleration of osteoblastic cell proliferation [136]. The chitosan has also been reported to support the expression of extracellular matrix proteins in osteoblasts and the preferential attachment of osteoblasts over other cell types [137].

It was observed that MC3T3-E1 cell attachment, viability and proliferation on the MAC and MAC-Lp scaffold could demonstrate the potential of the hydrogel application as a tissue culture scaffold.

With the development of 3D printing, methacrylated chitosan (MAC) hydrogel integration with laponite (MAC-Lp) and scaffold printing can be tailored to porosities, mechanical, rheological properties and stabilities in different applications. All of these engineering approaches show promise in 3D tissue engineering.

In future work, the MAC-Lp scaffold must be verified in in-vivo bone defects, and a better understanding of its mechanisms and biological effects must be analyzed by protein levels and gene expression of osteogenic markers in vitro. The degradation rate of chitosan can be studied with FITC. The amount of laponite can be changed and integrated with MAC hydrogels. The mechanical, rheological, and morphological properties and swelling can be studied and observed in vitro with different amounts of Laponite integrated into MAC hydrogels.

REFERENCES

1. Arpornmaeklong, P., et al., *Growth and differentiation of mouse osteoblasts on chitosan–collagen sponges.* International journal of oral and maxillofacial surgery, 2007. **36**(4): p. 328-337.
2. Clarke, B., *Normal bone anatomy and physiology.* Clinical journal of the American Society of Nephrology, 2008. **3**(Supplement 3): p. S131-S139.
3. Saxena, S., et al., *Development of a new polypropylene-based suture: plasma grafting, surface treatment, characterization, and biocompatibility studies.* Macromolecular bioscience, 2011. **11**(3): p. 373-382.
4. Chiarello, E., et al., *Autograft, allograft and bone substitutes in reconstructive orthopedic surgery.* Aging clinical and experimental research, 2013. **25**: p. S101-3.
5. Grove, J.R. and M. Hardy, *Autograft, allograft and xenograft options in the treatment of neglected Achilles tendon ruptures: a historical review with illustration of surgical repair.* Foot Ankle J, 2008. **1**(5): p. 1-10.
6. Peppas, N.A. and R. Langer, *New challenges in biomaterials.* Science-AAAS-Weekly Paper Edition-including Guide to Scientific Information, 1994. **263**(5154): p. 1715-1719.
7. Censi, R., et al., *A Printable Photopolymerizable Thermosensitive p (HPMAm-lactate)-PEG Hydrogel for Tissue Engineering.* Advanced Functional Materials, 2011. **21**(10): p. 1833-1842.
8. Kopeček, J. and J. Yang, *Hydrogels as smart biomaterials.* Polymer international, 2007. **56**(9): p. 1078-1098.

9. Anderson, J.M. and J.J. Langone, *Issues and perspectives on the biocompatibility and immunotoxicity evaluation of implanted controlled release systems.* Journal of controlled release, 1999. **57**(2): p. 107-113.

10. Vermonden, T., et al., *Photopolymerized thermosensitive hydrogels: synthesis, degradation, and cytocompatibility.* Biomacromolecules, 2008. **9**(3): p. 919-926.

11. Kopecek, J. and L. Sprincl, *Relationship between the structure and biocompatibility of hydrophilic gels.* Polimery w medycynie, 1974. **4**(2): p. 109-117.

12. Hoffman, A.S., *Hydrogels for biomedical applications.* Advanced drug delivery reviews, 2012. **64**: p. 18-23.

13. Kessler, M.W. and D.A. Grande, *Tissue engineering and cartilage.* Organogenesis, 2008. **4**(1): p. 28-32.

14. Tan, H., et al., *Injectable in situ forming biodegradable chitosan–hyaluronic acid based hydrogels for cartilage tissue engineering.* Biomaterials, 2009. **30**(13): p. 2499-2506.

15. Basavaraj, K., et al., *Biopolymers as transdermal drug delivery systems in dermatology therapy.* Critical Reviews™ in Therapeutic Drug Carrier Systems, 2010. **27**(2).

16. Helary, C., et al., *Concentrated collagen hydrogels as dermal substitutes.* Biomaterials, 2010. **31**(3): p. 481-490.

17. Hesse, E., et al., *Collagen type I hydrogel allows migration, proliferation, and osteogenic differentiation of rat bone marrow stromal cells.* Journal of Biomedical Materials Research Part A, 2010. **94**(2): p. 442-449.

18. Hunt, N.C. and L.M. Grover, *Cell encapsulation using biopolymer gels for regenerative medicine.* Biotechnology letters, 2010. **32**(6): p. 733-742.

19. van de Manakker, F., et al., *Protein-Release Behavior of Self-Assembled PEG–β-Cyclodextrin/PEG–Cholesterol Hydrogels.* Advanced Functional Materials, 2009. **19**(18): p. 2992-3001.

20. Bourke, S.L., et al., *A photo-crosslinked poly (vinyl alcohol) hydrogel growth factor release vehicle for wound healing applications.* The AAPS Journal, 2003. **5**(4): p. 101-111.

21. Lu, S. and K.S. Anseth, *Photopolymerization of multilaminated poly (HEMA) hydrogels for controlled release.* Journal of controlled release, 1999. **57**(3): p. 291-300.

22. Elisseeff, J., et al., *Synthesis and characterization of photo-cross-linked polymers based on poly (L-lactic acid-co-L-aspartic acid).* Macromolecules, 1997. **30**(7): p. 2182-2184.

23. Wangtueai, S. and A. Noomhorm, *Processing optimization and characterization of gelatin from lizardfish (Saurida spp.) scales.* LWT-Food Science and Technology, 2009. **42**(4): p. 825-834.

24. Ward, A.G. and A. Courts, *Science and technology of gelatin*. 1977: Academic Press.

25. Maurer, P.H., *II. Antigenicity of gelatin in rabbits and other species.* The Journal of experimental medicine, 1954. **100**(5): p. 515.

26. Zhu, J. and R.E. Marchant, *Design properties of hydrogel tissue-engineering scaffolds.* Expert review of medical devices, 2011. **8**(5): p. 607-626.

27. Haraguchi, K. and H.-J. Li, *Mechanical properties and structure of polymer− clay nanocomposite gels with high clay content.* Macromolecules, 2006. **39**(5): p. 1898-1905.

28. Tian, W., et al., *Hyaluronic acid–poly-D-lysine-based three-dimensional hydrogel for traumatic brain injury.* Tissue engineering, 2005. **11**(3-4): p. 513-525.

29. Clark, A., et al., *Structural and mechanical properties of agar/gelatin co-gels. Small-deformation studies.* Macromolecules, 1983. **16**(8): p. 1367-1374.

30. Yasuda, K., et al., *Biomechanical properties of high-toughness double network hydrogels.* Biomaterials, 2005. **26**(21): p. 4468-4475.

31. Elzoghby, A.O., *Gelatin-based nanoparticles as drug and gene delivery systems: reviewing three decades of research.* Journal of Controlled Release, 2013. **172**(3): p. 1075-1091.

32. Iyer, P., K.J. Walker, and S.V. Madihally, *Increased matrix synthesis by fibroblasts with decreased proliferation on synthetic chitosan–gelatin porous structures.* Biotechnology and bioengineering, 2012. **109**(5): p. 1314-1325.

33. Shigemasa, Y., et al., *Enzymatic degradation of chitins and partially deacetylated chitins.* International journal of biological macromolecules, 1994. **16**(1): p. 43-49.

34. Khor, E. and L.Y. Lim, *Implantable applications of chitin and chitosan.* Biomaterials, 2003. **24**(13): p. 2339-2349.

35. Madihally, S.V. and H.W. Matthew, *Porous chitosan scaffolds for tissue engineering.* Biomaterials, 1999. **20**(12): p. 1133-1142.

36. Suh, J.-K.F. and H.W. Matthew, *Application of chitosan-based polysaccharide biomaterials in cartilage tissue engineering: a review.* Biomaterials, 2000. **21**(24): p. 2589-2598.

37. Mi, F.-L., et al., *In vivo biocompatibility and degradability of a novel injectable-chitosan-based implant.* Biomaterials, 2002. **23**(1): p. 181-191.

38. Kristiansen, A., K.M. Vårum, and H. Grasdalen, *The interactions between highly de-N-acetylated chitosans and lysozyme from chicken egg white studied by 1H-NMR spectroscopy.* The FEBS Journal, 1998. **251**(1-2): p. 335-342.

39. Aiba, S.-i., et al., *Covalent immobilization of chitosan derivatives onto polymeric film surfaces with the use of a photosensitive hetero-bifunctional crosslinking reagent.* Biomaterials, 1987. **8**(6): p. 481-488.

40. Cai, K., et al., *Surface modification of poly (D, L-lactic acid) with chitosan and its effects on the culture of osteoblasts in vitro.* Journal of Biomedical Materials Research Part A, 2002. **60**(3): p. 398-404.

41. Lahiji, A., et al., *Chitosan supports the expression of extracellular matrix proteins in human osteoblasts and chondrocytes.* Journal of biomedical materials research, 2000. **51**(4): p. 586-595.

42. Arpornmaeklong, P., P. Pripatnanont, and N. Suwatwirote, *Properties of chitosan–collagen sponges and osteogenic differentiation of rat-bone-marrow stromal cells.* International journal of oral and maxillofacial surgery, 2008. **37**(4): p. 357-366.

43. Li, B., et al., *Gradient structural bone-like apatite induced by chitosan hydrogel via ion assembly.* Journal of Biomaterials Science, Polymer Edition, 2011. **22**(4-6): p. 505-517.

44. Jiang, T., W.I. Abdel-Fattah, and C.T. Laurencin, *In vitro evaluation of chitosan/poly (lactic acid-glycolic acid) sintered microsphere scaffolds for bone tissue engineering.* Biomaterials, 2006. **27**(28): p. 4894-4903.

45. Kim, I.-Y., et al., *Chitosan and its derivatives for tissue engineering applications.* Biotechnology advances, 2008. **26**(1): p. 1-21.

46. López-García, J., et al., *HaCaT keratinocytes response on antimicrobial atelocollagen substrates: extent of cytotoxicity, cell viability and proliferation.* Journal of functional biomaterials, 2014. **5**(2): p. 43-57.

47. Kokubo, T., H.-M. Kim, and M. Kawashita, *Novel bioactive materials with different mechanical properties.* Biomaterials, 2003. **24**(13): p. 2161-2175.

48. Bucholz, R.W., *Nonallograft osteoconductive bone graft substitutes.* Clinical orthopaedics and related research, 2002. **395**: p. 44-52.

49. Panetta, N.J., et al., *Tissue engineering in cleft palate and other congenital malformations.* Pediatric Research, 2008. **63**(5): p. 545-551.

50. Shih, T.C., et al., *In vivo evaluation of resorbable bone graft substitutes in beagles: histological properties.* Journal of Biomedical Materials Research Part A, 2013. **101**(8): p. 2405-2411.

51. Damien, C.J. and J.R. Parsons, *Bone graft and bone graft substitutes: a review of current technology and applications.* Journal of Applied Biomaterials, 1991. **2**(3): p. 187-208.

52. McCarthy, J.G., et al., *Distraction osteogenesis of the craniofacial skeleton.* Plastic and reconstructive surgery, 2001. **107**(7): p. 1812-1827.

53. Maehira, F., et al., *Effects of soluble silicon compound and deep-sea water on biochemical and mechanical properties of bone and the related gene expression in mice.* Journal of bone and mineral metabolism, 2008. **26**(5): p. 446-455.

54. Reffitt, D., et al., *Orthosilicic acid stimulates collagen type 1 synthesis and osteoblastic differentiation in human osteoblast-like cells in vitro.* Bone, 2003. **32**(2): p. 127-135.

55. Izu, A., et al., *Silicon intake to vertebral columns of mice after dietary supply.* Biological trace element research, 2006. **113**(3): p. 297-316.

56. Rahaman, M.N., et al., *Bioactive glass in tissue engineering.* Acta biomaterialia, 2011. **7**(6): p. 2355-2373.

57. Kobayashi, H., et al., *Evaluation of a silica-containing bone graft substitute in a vertebral defect model.* Journal of Biomedical Materials Research Part A, 2010. **92**(2): p. 596-603.

58. Feuille, F., et al., *Clinical and histologic evaluation of bone-replacement grafts in the treatment of localized alveolar ridge defects. Part 1: Mineralized freeze-dried bone allograft.* International Journal of Periodontics & Restorative Dentistry, 2003. **23**(1).

59. Zhao, S., et al., *Three-dimensional printed strontium-containing mesoporous bioactive glass scaffolds for repairing rat critical-sized calvarial defects.* Acta biomaterialia, 2015. **12**: p. 270-280.

60. Sui, B., G. Zhong, and J. Sun, *Evolution of a Mesoporous Bioactive Glass Scaffold Implanted in Rat Femur Evaluated by 45Ca Labeling, Tracing, and Histological Analysis.* ACS applied materials & interfaces, 2014. **6**(5): p. 3528-3535.

61. Van Olphen, H., *An introduction to clay colloid chemistry: for clay technologists, geologists, and soil scientists*. 1977.

62. Wu, C.-J., et al., *Development of biomedical polymer-silicate nanocomposites: a materials science perspective.* Materials, 2010. **3**(5): p. 2986-3005.

63. Bordes, P., E. Pollet, and L. Avérous, *Nano-biocomposites: biodegradable polyester/nanoclay systems.* Progress in Polymer Science, 2009. **34**(2): p. 125-155.

64. Xavier, J.R., et al., *Bioactive nanoengineered hydrogels for bone tissue engineering: a growth-factor-free approach.* ACS nano, 2015. **9**(3): p. 3109-3118.

65. Gaharwar, A.K., et al., *Bioactive silicate nanoplatelets for osteogenic differentiation of human mesenchymal stem cells.* Advanced materials, 2013. **25**(24): p. 3329-3336.

66. Thompson, D.W. and J.T. Butterworth, *The nature of laponite and its aqueous dispersions.* Journal of Colloid and Interface Science, 1992. **151**(1): p. 236-243.

67. Zulian, L., et al., *Dual aging behaviour in a clay–polymer dispersion.* Soft matter, 2014. **10**(25): p. 4513-4521.

68. Van Tomme, S.R., G. Storm, and W.E. Hennink, *In situ gelling hydrogels for pharmaceutical and biomedical applications.* International journal of pharmaceutics, 2008. **355**(1): p. 1-18.

69. Burdick, J.A., et al., *Controlled degradation and mechanical behavior of photopolymerized hyaluronic acid networks.* Biomacromolecules, 2005. **6**(1): p. 386-391.

70. Tai, H., et al., *Thermoresponsive and photocrosslinkable PEGMEMA-PPGMA-EGDMA copolymers from a one-step ATRP synthesis.* Biomacromolecules, 2009. **10**(4): p. 822-828.

71. Reddy, N., R. Reddy, and Q. Jiang, *Crosslinking biopolymers for biomedical applications.* Trends in biotechnology, 2015. **33**(6): p. 362-369.

72. Bryant, S.J., C.R. Nuttelman, and K.S. Anseth, *Cytocompatibility of UV and visible light photoinitiating systems on cultured NIH/3T3 fibroblasts in vitro.* Journal of Biomaterials Science, Polymer Edition, 2000. **11**(5): p. 439-457.

73. Sawhney, A.S., C.P. Pathak, and J.A. Hubbell, *Bioerodible hydrogels based on photopolymerized poly (ethylene glycol)-co-poly (. alpha.-hydroxy acid) diacrylate macromers.* Macromolecules, 1993. **26**(4): p. 581-587.

74. Jung, J. and J. Oh, *Swelling characterization of photo-cross-linked gelatin methacrylate spherical microgels for bioencapsulation.* e-Polymers, 2014. **14**(3): p. 161-168.

75. Lupovici, J., *Regeneration of the anterior mandible: a clinical case presentation.* JIRD, 2009. **1**: p. 31-34.

76. Varghese, D., et al., *Advances in tissue engineering: cell printing.* The Journal of thoracic and cardiovascular surgery, 2005. **129**(2): p. 470-472.

77. Fedorovich, N.E., et al., *Hydrogels as extracellular matrices for skeletal tissue engineering: state-of-the-art and novel application in organ printing.* Tissue engineering, 2007. **13**(8): p. 1905-1925.

78. Peltola, S.M., et al., *A review of rapid prototyping techniques for tissue engineering purposes.* Annals of medicine, 2008. **40**(4): p. 268-280.

79. Saraiva, S.M., et al., *Synthesis and characterization of a photocrosslinkable chitosan–gelatin hydrogel aimed for tissue regeneration.* Rsc Advances, 2015. **5**(78): p. 63478-63488.

80. Hutmacher, D.W., *Scaffolds in tissue engineering bone and cartilage.* Biomaterials, 2000. **21**(24): p. 2529-2543.

81. Bose, S., S. Vahabzadeh, and A. Bandyopadhyay, *Bone tissue engineering using 3D printing.* Materials Today, 2013. **16**(12): p. 496-504.

82. Cesarano III, J. and P.D. Calvert, *Freeforming objects with low-binder slurry*. 2000, Google Patents.

83. Lewis, J.A., et al., *Direct ink writing of three-dimensional ceramic structures.* Journal of the American Ceramic Society, 2006. **89**(12): p. 3599-3609.

84. Joshi, A.M., *Process planning for the rapid machining of custom bone implants*. 2011: Iowa State University.

85. Shao, H., et al., *3D robocasting magnesium-doped wollastonite/TCP bioceramic scaffolds with improved bone regeneration capacity in critical sized calvarial defects.* Journal of Materials Chemistry B, 2017. **5**(16): p. 2941-2951.

86. Olsen, B.R., A.M. Reginato, and W. Wang, *Bone development.* Annual review of cell and developmental biology, 2000. **16**(1): p. 191-220.

87. Yelin, E., *Cost of musculoskeletal diseases: impact of work disability and functional decline.* The Journal of Rheumatology Supplement, 2003. **68**: p. 8-11.

88. Arrington, E.D., et al., *Complications of iliac crest bone graft harvesting.* Clinical orthopaedics and related research, 1996. **329**: p. 300-309.

89. Beebe, D.J., et al., *Functional hydrogel structures for autonomous flow control inside microfluidic channels.* Nature, 2000. **404**(6778): p. 588.

90. Arakawa, C.K., *A Novel Photopolymerizable Chitosan Collagen Hydrogel for Bone Tissue Engineering.* 2012.

91. Hu, J., et al., *Visible light crosslinkable chitosan hydrogels for tissue engineering.* Acta biomaterialia, 2012. **8**(5): p. 1730-1738.

92. Salasznyk, R.M., et al., *Activation of FAK is necessary for the osteogenic differentiation of human mesenchymal stem cells on laminin-5.* Journal of cellular biochemistry, 2007. **100**(2): p. 499-514.

93. Zara, J.N., et al., *High doses of bone morphogenetic protein 2 induce structurally abnormal bone and inflammation in vivo.* Tissue Engineering Part A, 2011. **17**(9-10): p. 1389-1399.

94. Kim, H.-W., H.-E. Kim, and V. Salih, *Stimulation of osteoblast responses to biomimetic nanocomposites of gelatin–hydroxyapatite for tissue engineering scaffolds.* Biomaterials, 2005. **26**(25): p. 5221-5230.

95. Nichol, J.W., et al., *Cell-laden microengineered gelatin methacrylate hydrogels.* Biomaterials, 2010. **31**(21): p. 5536-5544.

96. Lu, S., et al., *Preparation of water-soluble chitosan.* Journal of Applied Polymer Science, 2004. **91**(6): p. 3497-3503.

97. Yu, L.M., K. Kazazian, and M.S. Shoichet, *Peptide surface modification of methacrylamide chitosan for neural tissue engineering applications.* Journal of Biomedical Materials Research Part A, 2007. **82**(1): p. 243-255.

98. Yu, L. and J. Ding, *Injectable hydrogels as unique biomedical materials.* Chemical Society Reviews, 2008. **37**(8): p. 1473-1481.

99. Nojoomi, A., et al., *Injectable polyethylene glycol-laponite composite hydrogels as articular cartilage scaffolds with superior mechanical and rheological properties.* International Journal of Polymeric Materials and Polymeric Biomaterials, 2017. **66**(3): p. 105-114.

100. Nojoomi, A., M. Faghihi-Sani, and M. Khoshkalam, *Shear-rate dependence modeling of gelcast slurries: Effects of dispersant content and solid loading.* Ceramics International, 2014. **40**(1): p. 123-128.

101. Shen, M., *Rheological properties of laponite and chemically modified laponite suspenisons*. 2014, Purdue University.

102. Meyvis, T.K., et al., *A comparison between the use of dynamic mechanical analysis and oscillatory shear rheometry for the characterisation of hydrogels.* International journal of pharmaceutics, 2002. **244**(1): p. 163-168.

103. Varanasi, V.G., et al., *In vivo live 3d printing of regenerative bone healing scaffolds for rapid fracture healing*. 2016, Google Patents.

104. Murphy, S.V. and A. Atala, *3D bioprinting of tissues and organs.* Nature biotechnology, 2014. **32**(8): p. 773-785.

105. Kozlov, P. and G. Burdygina, *The structure and properties of solid gelatin and the principles of their modification.* Polymer, 1983. **24**(6): p. 651-666.

106. Boral, S., A.N. Gupta, and H. Bohidar, *Swelling and de-swelling kinetics of gelatin hydrogels in ethanol–water marginal solvent.* International journal of biological macromolecules, 2006. **39**(4): p. 240-249.

107. Patel, R.G., et al., *Microscale bioadhesive hydrogel arrays for cell engineering applications.* Cellular and molecular bioengineering, 2014. **7**(3): p. 394-408.

108. Chiou, B.-S. and S.A. Khan, *Real-time FTIR and in situ rheological studies on the UV curing kinetics of thiol-ene polymers.* Macromolecules, 1997. **30**(23): p. 7322-7328.

109. Callister, W.D. and D.G. Rethwisch, *Materials science and engineering*. Vol. 5. 2011: John Wiley & Sons NY.

110. Goldstein, J., et al., *Scanning electron microscopy and X-ray microanalysis: a text for biologists, materials scientists, and geologists*. 2012: Springer Science & Business Media.

111. Käppler, A., et al., *Identification of microplastics by FTIR and Raman microscopy: a novel silicon filter substrate opens the important spectral range below 1300 cm− 1 for*

FTIR transmission measurements. Analytical and bioanalytical chemistry, 2015. **407**(22): p. 6791-6801.

112. März, A., et al., *Droplet formation via flow-through microdevices in Raman and surface enhanced Raman spectroscopy—concepts and applications.* Lab on a Chip, 2011. **11**(21): p. 3584-3592.

113. Mano, N., F. Mao, and A. Heller, *Characteristics of a miniature compartment-less glucose− O2 biofuel cell and its operation in a living plant.* Journal of the American Chemical Society, 2003. **125**(21): p. 6588-6594.

114. Marchessault, R.H., F. Ravenelle, and X.X. Zhu, *Polysaccharides for drug delivery and pharmaceutical applications*. 2006: ACS Publications.

115. Darder, A., *The critical pedagogy reader*. 2003: Psychology Press.

116. Han, J., T. Lei, and Q. Wu, *High-water-content mouldable polyvinyl alcohol-borax hydrogels reinforced by well-dispersed cellulose nanoparticles: Dynamic rheological properties and hydrogel formation mechanism.* Carbohydrate polymers, 2014. **102**: p. 306-316.

117. Yang, H., et al., *Composite hydrogel beads based on chitosan and laponite: preparation, swelling, and drug release behaviour.* Iran Polym J, 2011. **20**(6): p. 479-490.

118. Gaharwar, A.K., et al., *Addition of chitosan to silicate cross-linked PEO for tuning osteoblast cell adhesion and mineralization.* ACS applied materials & interfaces, 2010. **2**(11): p. 3119-3127.

119. Shen, M., et al., *Rheology and adhesion of poly (acrylic acid)/laponite nanocomposite hydrogels as biocompatible adhesives.* Langmuir, 2014. **30**(6): p. 1636-1642.

120. Gaharwar, A.K., et al., *Physically Crosslinked Nanocomposites from Silicate-Crosslinked PEO: Mechanical Properties and Osteogenic Differentiation of Human Mesenchymal Stem Cells.* Macromolecular bioscience, 2012. **12**(6): p. 779-793.

121. Thein-Han, W., et al., *Chitosan–gelatin scaffolds for tissue engineering: Physico-chemical properties and biological response of buffalo embryonic stem cells and transfectant of GFP–buffalo embryonic stem cells.* Acta biomaterialia, 2009. **5**(9): p. 3453-3466.

122. Gaharwar, A.K., et al., *Transparent, elastomeric and tough hydrogels from poly (ethylene glycol) and silicate nanoparticles.* Acta biomaterialia, 2011. **7**(12): p. 4139-4148.

123. Hutson, C.B., et al., *Synthesis and characterization of tunable poly (ethylene glycol): gelatin methacrylate composite hydrogels.* Tissue Engineering Part A, 2011. **17**(13-14): p. 1713-1723.

124. Cordier, P., et al., *Self-healing and thermoreversible rubber from supramolecular assembly.* Nature, 2008. **451**(7181): p. 977.

125. Chen, P.-Y. and J. McKittrick, *Compressive mechanical properties of demineralized and deproteinized cancellous bone.* Journal of the mechanical behavior of biomedical materials, 2011. **4**(7): p. 961-973.

126. Wang, J., J. de Boer, and K. De Groot, *Proliferation and differentiation of MC3T3-E1 cells on calcium phosphate/chitosan coatings.* Journal of dental research, 2008. **87**(7): p. 650-654.

127. Xiaoyu, Z., et al., *1α, 25 (OH) 2-vitamin D 3 membrane-initiated calcium signaling modulates exocytosis and cell survival.* The Journal of steroid biochemistry and molecular biology, 2007. **103**(3): p. 457-461.

128. Uygun, A., et al., *RF hydrazine plasma modification of chitosan for antibacterial activity and nanofiber applications.* Carbohydrate research, 2011. **346**(2): p. 259-265.

129. Cárdenas, G., et al., *Chitosan composite films. Biomedical applications.* Journal of Materials Science: Materials in Medicine, 2008. **19**(6): p. 2397-2405.

130. Pleshko, N., A. Boskey, and R. Mendelsohn, *Novel infrared spectroscopic method for the determination of crystallinity of hydroxyapatite minerals.* Biophysical journal, 1991. **60**(4): p. 786-793.

131. Peter, M., et al., *Preparation and characterization of chitosan–gelatin/nanohydroxyapatite composite scaffolds for tissue engineering applications.* Carbohydrate Polymers, 2010. **80**(3): p. 687-694.